Konrad-Zuse-Zentrum
für Informationstechnik Berlin

Takustraße 7
D-14195 Berlin-Dahlem
Germany

RUDOLF BECK [1] PETER DEUFLHARD [2] RALF HIPTMAIR [3]
RONALD H.W. HOPPE [4] BARBARA WOHLMUTH [5]

Adaptive Multilevel Methods for Edge Element Discretizations of Maxwell's Equations

[1] Konrad-Zuse-Zentrum für Informationstechnik Berlin, e-mail: Beck@zib.de
[2] Konrad-Zuse-Zentrum für Informationstechnik Berlin, e-mail: Deuflhard@zib.de
[3] Institut für Mathematik, Universität Augsburg, e-mail: Hiptmair@math.uni-augsburg.de
[4] Institut für Mathematik, Universität Augsburg, e-mail: Hoppe@math.uni-augsburg.de
[5] Institut für Mathematik, Universität Augsburg, currently at Courant Institute of Mathematical Sciences, New York, e-mail: Wohlmuth@cs.nyu.edu

Preprint SC 97-66 (December 1997)

Adaptive Multilevel Methods for Edge Element Discretizations of Maxwell's Equations

Rudolf Beck Peter Deuflhard Ralf Hiptmair
Ronald H.W. Hoppe Barbara Wohlmuth

Abstract

The focus of this paper is on the efficient solution of boundary value problems involving the double–**curl** operator. Those arise in the computation of electromagnetic fields in various settings, for instance when solving the electric or magnetic wave equation with implicit timestepping, when tackling time–harmonic problems or in the context of eddy–current computations.

Their discretization is based on on Nédélec's $\boldsymbol{H}(\mathbf{curl};\Omega)$-conforming edge elements on unstructured grids. In order to capture local effects and to guarantee a prescribed accuracy of the approximate solution adaptive refinement of the grid controlled by a posteriori error estimators is employed. The hierarchy of meshes created through adaptive refinement forms the foundation for the fast iterative solution of the resulting linear systems by a multigrid method.

The guiding principle underlying the design of both the error estimators and the multigrid method is the separate treatment of the kernel of the **curl**–operator and its orthogonal complement. Only on the latter we have proper ellipticity of the problem. Yet, exploiting the existence of computationally available discrete potentials for edge element spaces, we can switch to an elliptic problem in potential space to deal with nullspace of **curl**. Thus both cases become amenable to strategies of error estimation and multigrid solution developed for second order elliptic problems.

The efficacy of the approach is confirmed by numerical experiments which cover several model problems and an application to waveguide simulation.

Key words. Maxwell's equations, edge elements, Nédélec's elements, multigrid methods, a posteriori error estimators, waveguide simulation

AMS(MOS) subject classifications. 65N55, 65N30, 65P05, 35Q60

1 Introduction

The past decades have seen the development of a vast array of numerical techniques for the computation of electromagnetic fields, accompanied by the arrival of ever more powerful computer hardware. This has made possible the fast and accurate prediction of electromagnetic phenomena and thus numerical simulation has emerged as an indispensable tool for the analysis and the design of technical devices in electrical engineering.

Basically, there is a single set of equations governing all electromagnetic phenomena, *Maxwell's equations*. They comprise four first order partial differential equations linking the fundamental electromagnetic quantities, the electric field $\boldsymbol{E} = \boldsymbol{E}(\boldsymbol{x}, t)$, the magnetic induction $\boldsymbol{B} = \boldsymbol{B}(\boldsymbol{x}, t)$, the magnetic field $\boldsymbol{H} = \boldsymbol{H}(\boldsymbol{x}, t)$, the electric flux density $\boldsymbol{D} = \boldsymbol{D}(\boldsymbol{x}, t)$, the electric current $\boldsymbol{j} = \boldsymbol{j}(\boldsymbol{x}, t)$ and the space charge density $\rho = \rho(\boldsymbol{x}, t)$:

$$\mathbf{curl}\, \boldsymbol{H} = \boldsymbol{j} + \partial_t \boldsymbol{D} \qquad \operatorname{div} \boldsymbol{D} = \rho \tag{1}$$

$$\mathbf{curl}\, \boldsymbol{E} = -\partial_t \boldsymbol{B} \qquad \operatorname{div} \boldsymbol{B} = 0 \tag{2}$$

Strictly speaking, these equations are posed over the entire space $\mathbb{R}^3$ and they have to be supplemented by the following material laws:

$$\boldsymbol{D} = \epsilon \boldsymbol{E}\ , \qquad \boldsymbol{B} = \mu \boldsymbol{H}\ , \qquad \boldsymbol{j} = \sigma \boldsymbol{E} + \boldsymbol{j}_i\ , \tag{3}$$

where $\boldsymbol{j}_i$ denotes an intrinsic current density. The combined equations (1)–(3) form a second order hyperbolic system describing the behavior of electromagnetic waves and their interaction with matter. In this presentation we admit only linear and isotropic materials, in which case ϵ, μ, σ are bounded scalar functions of the spatial variable $\boldsymbol{x}$ with $\epsilon \geq \epsilon_0 > 0$, $\mu \geq \mu_0 > 0$ and $\sigma \geq 0$ almost everywhere. As a matter of course, steep jumps in these coefficients may occur at material interfaces.

In principle, all computations of electromagnetic fields could be tackled by a general purpose solver for Maxwell's equations. Yet, in special situations additional assumptions allow substantial simplifications of the model. Most of these assumptions concern the temporal variation of the fields:

In the *stationary case* we encounter the familiar problems of electro– and magnetostatics. The mathematical models boil down to elliptic boundary value problems corresponding to a minimization of energy or energy dissipation, respectively. In general, methods working with electric and magnetic potentials are preferred in these cases [87].

In the case of *time–harmonic processes* and linear material properties, we can switch to the frequency domain and end up with indefinite second order problems in space for the complex amplitudes of the fields. This approach is feasible for a wide range of scattering problems, waveguide computations [61, 87] and the determination of propagating modes, where the latter application involves the solution of an eigenvalue problem [41].

Transient, slowly–varying fields permit us to ignore wave propagation [28]. Crudely speaking, this yields a reasonable approximation provided that possibly occurring electromagnetic waves possess a wavelength much greater than the size of the region of

interest. Situations where this requirement is met often include eddy–current simulations, for instance in electrical engines and transformers [17, 18, 65]. Then we typically arrive at problems of parabolic type.

If *transient, fast processes* are involved we have to resort to the full Maxwell's equations, which may be converted into a wave equation for either the electric or magnetic field. This is necessary for an adequate modeling of certain scattering problems which are typically appearing in microwave structures [64, 66].

The bottom line is that the mathematical features of the models for electromagnetic fields crucially depend on the kind of simplification employed. A crude distinction can be made between equilibrium and near–equilibrium situations, typical of low–frequency settings, and arrangements where wave propagation is the principal effect. The former case gives rise to elliptic or parabolic problems, whereas the latter leads to hyperbolic equations.

Matching the diversity of situations, numerous different approaches have been devised for the numerical treatment of the electromagnetic problems:

Temporal discretization can be done in an explicit fashion only in the pronounced hyperbolic case, for example, by means of the popular leap–frog scheme [69, 98]. Otherwise we are faced with stiff problems, which require implicit schemes in order to avoid severe limitations on the length of admissible timesteps due to the well–known CFL–restriction. These methods entail solving a stationary boundary value problem in each timestep.

Several approaches have been explored for the *spatial discretization* of the field equations. The first schemes to be used in practical codes were *finite difference techniques* [93, 98], which approximate the electromagnetic fields in regularly arranged gridpoints (nodes) and express the discrete differential operator by algebraic equations linking neighboring nodes. Closely related are generalized finite volume methods, like the finite integration technique [91, 92]. The fairly regular hexahedral grids employed allow for easy implementation. In particular, in connection with explicit timestepping finite difference methods are fairly popular [35, 101].

Finite elements [33, 61, 103] provide an alternative discretization in space. They rely on approximation spaces for the physical quantities that possess locally supported basis functions with respect to a triangulation of a bounded computational domain. Finite element discretizations can cope well with unstructured meshes and offer enhanced flexibility compared to finite difference methods.

A completely different kind of spatial discretization can be achieved by means of *boundary element methods* [63, 86]. The boundary value problem is converted into an integral equation for unknown functions on the boundary of the computational domain. Thanks to a reduction in the dimension of the problem we need to deal with a significantly reduced number of unknowns. Yet, this advantage is offset by the computational cost for the generation of the full system matrix and the solution of the discrete linear problem. In addition, it is difficult to apply the method to the case of non–constant material coefficients and non–linear problems. Nevertheless boundary elements are widely used in electromagnetic simulations, in particular, in combination with finite elements [26, 83].

In this paper, we only consider cases that lead to stationary second order boundary value problems for a *double–***curl** *operator*. We expose how advanced adaptive multilevel schemes, a cutting–edge numerical technology for second order elliptic problems,

can be adjusted to **curl curl**–problems. We summarize and extend results scattered over several recent publications by the authors [10–12, 54, 55]. What is entirely new is the comprehensive discussion of both error estimation and multigrid schemes for $\boldsymbol{H}(\mathbf{curl};\Omega)$–conforming finite elements.

Those arise in virtually all of the above mentioned settings, as we will reveal in Sect. 2. In that section we derive weak formulations posed over the Hilbert–space $\boldsymbol{H}(\mathbf{curl};\Omega)$ from Maxwell's equations. Sect. 3 is devoted to the discretization of the linear variational problems by means of $\boldsymbol{H}(\mathbf{curl};\Omega)$–conforming *edge elements*. In Sect. 4 we introduce a key concept for the design of both error estimators and multilevel iterative solvers, the *Helmholtz–decomposition* of $\boldsymbol{H}(\mathbf{curl};\Omega)$ and its finite element subspaces. The fifth section outlines the main principles of adaptive multilevel methods. One of their principal components, suitable *a–posteriori error estimators*, will be examined in the following section. After that, we deal with the second key component, fast *multigrid methods* for the solution of the large sparse linear systems of equations that result from the finite element discretization. In Sect. 8 we supply results from a number of numerical experiments and discuss real–life simulation.

In this presentation the emphasis is on the fundamental principles of error estimators and multilevel schemes and the key role played by specific properties of the edge element approximation. We largely dispense with rigorous proofs and prefer heuristic arguments to motivate the design of the algorithms. We aim to drive home our conviction that the techniques, ranging from the finite element approximation to multigrid solvers, are "naturally" stipulated by the structure of the problem.

2 Variational formulations

In this section we focus on the weak formulation of Maxwell's equations, that is, we convert them into variational equations posed over suitable function spaces. An adequate choice for these function spaces are vectorfields of finite energy, for which the application of the differential operators is "meaningful". In other words, applying **curl** and div must not lead to unbounded energy. Remember that the energy of the fields is measured through weighted L^2–norms. This hints that the appropriate spaces for the electric field $\boldsymbol{E}$ and the magnetic field $\boldsymbol{H}$ are provided by

$$\boldsymbol{H}(\mathbf{curl};\Omega) := \{\boldsymbol{\eta} \in \boldsymbol{L}^2(\Omega)\,;\ \mathbf{curl}\,\boldsymbol{\eta} \in \boldsymbol{L}^2(\Omega)\}\ .$$

Here $\Omega \subset \mathbb{R}^3$ is a domain, not necessarily bounded, whose boundary $\partial\Omega$, if non–empty, is sufficiently regular (Lipschitz–continuous). Similarly, we define the function space

$$\boldsymbol{H}(\mathrm{div};\Omega) := \{\boldsymbol{v} \in \boldsymbol{L}^2(\Omega)\,;\ \mathrm{div}\,\boldsymbol{v} \in L^2(\Omega)\}\ ,$$

to which the displacement current $\boldsymbol{D}$ and the magnetic induction $\boldsymbol{B}$ should belong. Both spaces, equipped with the canonical inner products, are Hilbert–spaces with norms

$$\|\boldsymbol{\xi}\|^2_{\boldsymbol{H}(\mathbf{curl};\Omega)} := \|\boldsymbol{\xi}\|^2_{0;\Omega} + \|\mathbf{curl}\,\boldsymbol{\xi}\|^2_{0;\Omega} \tag{4}$$

$$\|\boldsymbol{v}\|^2_{\boldsymbol{H}(\mathrm{div};\Omega)} := \|\boldsymbol{v}\|^2_{0;\Omega} + \|\mathrm{div}\,\boldsymbol{v}\|^2_{0;\Omega}\ . \tag{5}$$

We write $\|\cdot\|_{0;\Omega}$ for the $L^2(\Omega)$–norm and $(\cdot,\cdot)_{0;\Omega}$ for the $L^2(\Omega)$ inner product.

The subspace of $\boldsymbol{H}(\mathbf{curl};\Omega)$ containing the vectorfields $\boldsymbol{\xi}$ with vanishing tangential trace $\boldsymbol{\xi}\times\boldsymbol{n}$ on $\Gamma\subset\partial\Omega$ is denoted by $\boldsymbol{H}_\Gamma(\mathbf{curl};\Omega)$. As usual, $\boldsymbol{n}$ designates the exterior unit normal vectorfield on $\partial\Omega$. For a detailed discussion of the properties of these spaces the reader should consult [49, Ch. 1]. Throughout this presentation, unless the physical meaning of quantities suggests otherwise, small boldface Greek letters will stand for vectorfields from $\boldsymbol{H}(\mathbf{curl};\Omega)$, whereas those in $\boldsymbol{H}(\mathrm{div};\Omega)$ are tagged by small boldface Roman symbols.

A vexing question emerges: How should the material laws (3) be read, since they link functions from different spaces? To view them as mere scaling is obviously flawed. This reflects the widely shared perception that the material laws mar the consistency of Maxwell's equations; they arise from averaging and only make sense on a macroscopic scale. Thus, they are fittingly stated as equations involving weighted local averages. Unfortunately, there are two competing formulations for each material law and both are justified and problematic alike [26, 27]. For instance, $\boldsymbol{D}=\epsilon\boldsymbol{E}$ may be stated as

$$\begin{aligned}\left(\epsilon^{-1}\boldsymbol{D},\boldsymbol{v}\right)_{0;\Omega} &= (\boldsymbol{E},\boldsymbol{v})_{0;\Omega} \quad \forall\boldsymbol{v}\in\boldsymbol{H}(\mathrm{div};\Omega) &(6)\\ (\boldsymbol{D},\boldsymbol{\eta})_{0;\Omega} &= (\epsilon\boldsymbol{E},\boldsymbol{\eta})_{0;\Omega} \quad \forall\boldsymbol{\eta}\in\boldsymbol{H}(\mathbf{curl};\Omega) &(7)\end{aligned}$$

Note that we formulated the products in this way to achieve some formal consistency within the framework of differential geometry (see e.g. [24, 27]). Here the fields are interpreted as differential forms, products between 1-forms into 2-forms yielding electric or magnetic energy, respectively. The "coefficients" ϵ, μ and σ are operators transforming between differential forms of different order.

2.1 The high frequency transient case

There are several, by and large symmetric, ways to derive variational equations from (1), (2). We single out an approach that retains the electric field $\boldsymbol{E}$ as unknown. Alternatively we could zero in on the magnetic field [69] or handle a first order system [70]. First we get from (2)

$$\left(\mu^{-1}\,\mathbf{curl}\,\boldsymbol{E},\boldsymbol{v}\right)_{0;\Omega} = -\left(\mu^{-1}\partial_t\boldsymbol{B},\boldsymbol{v}\right)_{0;\Omega} \quad \forall\boldsymbol{v}\in\boldsymbol{H}(\mathrm{div};\Omega)\;, \tag{8}$$

which preserves (2) in strong form. Next, we plug in the material law $\boldsymbol{B}=\mu\boldsymbol{H}$ and set $\boldsymbol{v}=\mathbf{curl}\,\boldsymbol{\eta}$:

$$\left(\mu^{-1}\,\mathbf{curl}\,\boldsymbol{E},\mathbf{curl}\,\boldsymbol{\eta}\right)_{0;\Omega} = -\left(\partial_t\boldsymbol{H},\mathbf{curl}\,\boldsymbol{\eta}\right)_{0;\Omega} \quad \forall\boldsymbol{\eta}\in\boldsymbol{H}(\mathbf{curl};\Omega) \tag{9}$$

By means of a variant of Green's formula we derive the weak form of (1):

$$(\boldsymbol{H},\mathbf{curl}\,\boldsymbol{\eta})_{0;\Omega} + (\boldsymbol{H}\times\boldsymbol{n},\boldsymbol{\eta})_{0;\partial\Omega} = (\boldsymbol{j}+\partial_t\boldsymbol{D},\boldsymbol{\eta})_{0;\Omega} \quad \forall\boldsymbol{\eta}\in\boldsymbol{H}(\mathbf{curl};\Omega) \tag{10}$$

Using the material law $\boldsymbol{H}=\mu^{-1}\boldsymbol{B}$ again, we get from (9) and (10)

$$\left(\mu^{-1}\,\mathbf{curl}\,\boldsymbol{E},\mathbf{curl}\,\boldsymbol{\eta}\right)_{0;\Omega} = -\left(\boldsymbol{j}+\partial_t^2\boldsymbol{D},\boldsymbol{\eta}\right)_{0;\Omega} + (\partial_t\boldsymbol{H}\times\boldsymbol{n},\boldsymbol{\eta})_{0;\partial\Omega}\;.$$

Now Ohm's law $\boldsymbol{j} = \sigma \boldsymbol{E}$ can be applied along with (7) and $\boldsymbol{B} = \mu \boldsymbol{H}$, which are used to rephrase the boundary terms. This means that for all $\boldsymbol{\eta} \in \boldsymbol{H}(\mathbf{curl}; \Omega)$

$$\left(\epsilon \partial_t^2 \boldsymbol{E} + \sigma \partial_t \boldsymbol{E}, \boldsymbol{\eta}\right)_{0;\Omega} + \left(\mu^{-1} \mathbf{curl}\, \boldsymbol{E}, \mathbf{curl}\, \boldsymbol{\eta}\right)_{0;\Omega} + \left(\mu^{-1} \mathbf{curl}\, \boldsymbol{E} \times \boldsymbol{n}, \boldsymbol{\eta}\right)_{0;\partial\Omega} = -\left(\partial_t \boldsymbol{j}_i, \boldsymbol{\eta}\right)_{0;\Omega} .$$

This is the general weak form of the "electric" vector wave equation. Strictly speaking, this equation has to be considered on the entire space $\mathbb{R}^3$, seeking solutions that vanish at infinity. However, in practical computations, unless infinite elements [50, Sect. 6] or boundary element methods are employed, we can only deal with bounded computational domains. This entails supplying suitable boundary conditions to ensure uniqueness of the solution. The simplest method is to truncate the grid at some distance from the regions of interest and to assume an enclosure provided by a perfectly conducting material, which is equivalent to imposing vanishing tangential components of $\boldsymbol{E}$. Of course, such an arbitrary truncation will lead to undesired reflections of outgoing waves. Sophisticated investigations have been carried to remedy this drawback by so–called absorbing boundary conditions (ABC's) [38, 50]. In their first-order form such formulations realize Sommerfeld's radiation condition. For the electric field they read

$$\mathbf{curl}\, \boldsymbol{E} \times \boldsymbol{n} = (\boldsymbol{n} \times c^{-1} \partial_t \boldsymbol{E}) \times \boldsymbol{n} + \boldsymbol{E}_{\mathrm{inc}} \times \boldsymbol{n} \,, \tag{11}$$

where c denotes the phase velocity and is given by $c = \epsilon \mu^{-1/2}$. Equation (11) is a Cauchy–type boundary condition supposed to hold on $\Gamma_A := \partial\Omega / \Gamma_D$. Higher-order formulations have been developed in order to minimize artificial reflections [44, 77]. Another promising approach uses so–called perfectly matched layers (PML's), where the domain is covered by an anisotropic absorbing material [15].

We can now incorporate the boundary conditions into the variational equation and end up with the following initial boundary value problem describing the behavior of the electric field for times $t \in]0; T[$:

Seek $\boldsymbol{E} \in C^2([0;T], \boldsymbol{H}_{\Gamma_D}(\mathbf{curl}; \Omega))$ such that

$$\left(\epsilon \partial_t^2 \boldsymbol{E} + \sigma \partial_t \boldsymbol{E}, \boldsymbol{\eta}\right)_{0;\Omega} + \left(\mu^{-1} \mathbf{curl}\, \boldsymbol{E}, \mathbf{curl}\, \boldsymbol{\eta}\right)_{0;\Omega} - \left((\mu c)^{-1} \partial_t \boldsymbol{E} \times \boldsymbol{n}, \boldsymbol{\eta} \times \boldsymbol{n}\right)_{0;\Gamma_A} = -\left(\partial_t \boldsymbol{j}_i, \boldsymbol{\eta}\right)_{0;\Omega} + \left(\mu^{-1} \boldsymbol{E}_{\mathrm{inc}}, \boldsymbol{\eta}\right)_{0;\Gamma_A} \quad \forall \boldsymbol{\eta} \in \boldsymbol{H}_{\Gamma_D}(\mathbf{curl}; \Omega) \tag{12}$$

and fulfilling the initial condition $\boldsymbol{E}_{|t=0} = \boldsymbol{E}_0$ ($\operatorname{div} \boldsymbol{E}_0 = 0$).

This comprehensive model has to be used for the accurate simulation of transient electromagnetic phenomena, if wave propagation is a crucial feature.

In general, explicit timestepping schemes are the method of choice for the simulation of fast–scale transient electromagnetic phenomena, since timestep have to be kept small in order to curb numerical dispersion [75]. However to circumvent the CFL–condition, which may impose needlessly severe limitations on the maximal length of timesteps, we have to resort to implicit timestepping. In particular, in the case of lossy media ($\sigma > 0$) this is the only feasible option. Employing, for instance, the popular Crank–Nicholson scheme (Implicit trapezoidal rule), in each timestep we face the following stationary problem:

Seek $\boldsymbol{E}_n \in \boldsymbol{H}_{\Gamma_D}(\mathbf{curl};\Omega)$ such that for all $\boldsymbol{\eta} \in \boldsymbol{H}_{\Gamma_D}(\mathbf{curl};\Omega)$

$$\left((\epsilon + \frac{1}{2}\sigma\Delta t)\boldsymbol{E}_n, \boldsymbol{\eta}\right)_{0;\Omega} + \left(\frac{\Delta t^2}{4\mu}\,\mathbf{curl}\,\boldsymbol{E}_n, \mathbf{curl}\,\boldsymbol{\eta}\right)_{0;\Omega} - \\ - \left(\frac{\alpha\Delta t^2}{4\mu c}\partial_t \boldsymbol{E}\times\boldsymbol{n}, \boldsymbol{\eta}\times\boldsymbol{n}\right)_{0;\Gamma_A} = f(\boldsymbol{\eta})\;, \tag{13}$$

where $\Delta t > 0$ is the fixed length of the timesteps, $\boldsymbol{E}_n$ stands for the unknown electric field in the nth step and f is a functional on $\boldsymbol{H}_{\Gamma_D}(\mathbf{curl};\Omega)$, which comprises all excitations and, in addition, depends on the approximations $\boldsymbol{E}_{n-1}$, $\boldsymbol{E}_{n-2}$ in the previous timesteps. For a study of a wider class of implicit timestepping schemes see [67]. Formally speaking, (13) is a second order $\boldsymbol{H}(\mathbf{curl};\Omega)$–elliptic variational problem.

2.2 The eddy–current approximation

A significant simplification of (12) can be achieved for transient processes on a slow timescale in the presence of considerable dissipation, i.e. $\sigma > 0$. This is typical of eddy–current problems which deal with currents caused by slowly varying electromagnetic fields. Then wave propagation can be neglected and homogeneous boundary conditions also make sense for artificial boundaries. For the resulting parabolic problem, implicit timestepping is mandatory. For instance, when applying the implicit Euler scheme in the nth timestep we confront the variational problem

Seek $\boldsymbol{E}_n \in \boldsymbol{H}_0(\mathbf{curl};\Omega)$ such that for all $\boldsymbol{\eta} \in \boldsymbol{H}_0(\mathbf{curl};\Omega)$

$$(\sigma\boldsymbol{E}_n, \boldsymbol{\eta})_{0;\Omega} + \left(\Delta t\mu^{-1}\,\mathbf{curl}\,\boldsymbol{E}_n, \mathbf{curl}\,\boldsymbol{\eta}\right)_{0;\Omega} = f(\boldsymbol{\eta})\;, \tag{14}$$

where f is some right hand side functional, depending on known data and the length Δt of the timestep. This problem much resembles (12), but the uniqueness of the solution of (14) is not guaranteed in Ω_I, since there may be a non-conducting ($\sigma = 0$) region Ω_I. A possible remedy is to impose the *gauge condition* $\operatorname{div}\epsilon\boldsymbol{E} = 0$ in its weak form:

$$\left(\epsilon\boldsymbol{E}, \boldsymbol{\eta}^0\right)_{0;\Omega} = 0 \quad \forall\boldsymbol{\eta} \in \boldsymbol{H}_0^0(\mathbf{curl};\Omega_I)\;, \tag{15}$$

where $\boldsymbol{H}_0^0(\mathbf{curl};\Omega_I) := \{\boldsymbol{\eta} \in \boldsymbol{H}_0(\mathbf{curl};\Omega_I),\ \mathbf{curl}\,\boldsymbol{\eta} = 0 \text{ in } \Omega_I\}$ (In the sequel we are going to tag spaces of irrotational vectorfield by a superscript 0.).

We point out that apart from (14), (15) there are several alternative variational formulations of the eddy–current problem utilizing various scalar and vector potentials (see e.g. [17, 19]). Regardless of the model used, the governing equations for the vector potentials give rise to problems similar to (14).

2.3 The time–harmonic case

Now, all the quantities occurring in Maxwell's equations (1), (2) are assumed to feature a sinusoidal dependence on time with a fixed angular frequency $\omega > 0$. Then, we have the representation

$$\boldsymbol{E}(\boldsymbol{x},t) = \Re\left(\widehat{\boldsymbol{E}}(\boldsymbol{x})\exp(i\omega t)\right) \qquad \boldsymbol{x}\in\Omega, t\in\mathbb{R}\;,$$

with a *complex* amplitude $\widehat{\boldsymbol{E}} \in \boldsymbol{H}_{\Gamma_D}(\mathbf{curl};\Omega)$. Thus we can switch to the frequency domain and end up with [25, 71]:

Seek $\widehat{\boldsymbol{E}} \in \boldsymbol{H}_{\Gamma_D}(\mathbf{curl};\Omega)$ such that

$$\left(\mu^{-1}\,\mathbf{curl}\,\widehat{\boldsymbol{E}},\mathbf{curl}\,\widehat{\boldsymbol{\eta}}\right)_{0;\Omega} - \left(\omega^2\epsilon'\widehat{\boldsymbol{E}},\widehat{\boldsymbol{\eta}}\right)_{0;\Omega} - \left(\frac{i\omega}{\mu c}\widehat{\boldsymbol{E}}\times\boldsymbol{n},\widehat{\boldsymbol{\eta}}\times\boldsymbol{n}\right)_{0;\Gamma_A} = \widehat{f}(\widehat{\boldsymbol{\eta}}) \qquad (16)$$

for all (complex–valued) test functions $\widehat{\boldsymbol{\eta}} \in \boldsymbol{H}_{\Gamma_D}(\mathbf{curl};\Omega)$ and some functional $f \in \boldsymbol{H}_{\Gamma_D}(\mathbf{curl};\Omega)'$. The coefficient $\epsilon' := \epsilon - \sigma/i\omega$ stands for a complex dielectric constant. In this presentation we will consider the time–harmonic problem only for lossless media, i.e. $\sigma = 0$, which renders $\epsilon' = \epsilon$. However, we want to stress that the methods exposed in this paper work for the general case as well.

In contrast to the previous cases, the symmetric variational problem(16) is indefinite due to the negative weight of the zero order term. Moreover, (16) may not have a solution at all, if ω^2 happens to be equal to an eigenvalue of the $\mathbf{curl}\,\frac{1}{\mu}\,\mathbf{curl}$–operator. For a detailed discussion concerning existence and uniqueness of solutions we refer to [25, 28]. For the remainder of the paper we will take for granted that (16) has a unique solution.

Let us summarize the different models: In each case we finally came across a variational problem of the form:

Seek $\boldsymbol{E} \in \boldsymbol{H}_{\Gamma_D}(\mathbf{curl};\Omega)$, real valued or complex valued respectively, such that

$$a(\boldsymbol{E},\boldsymbol{\eta}) := (\alpha\,\mathbf{curl}\,\boldsymbol{\xi},\mathbf{curl}\,\boldsymbol{\eta})_{0;\Omega} + (\beta\boldsymbol{E},\boldsymbol{\eta})_{0;\Omega} + (\gamma\boldsymbol{E}\times\boldsymbol{n},\boldsymbol{\eta}\times\boldsymbol{n})_{0;\Gamma_A} = f(\boldsymbol{\eta}) \qquad (17)$$

for all $\boldsymbol{\eta} \in \boldsymbol{H}_{\Gamma_D}(\mathbf{curl};\Omega)$ and a suitable right hand side $f(\boldsymbol{\eta}) = (\boldsymbol{f},\boldsymbol{\eta})_{0;\Omega}$ with $\boldsymbol{f} \in \boldsymbol{L}^2(\Omega)$.

Throughout, $\alpha \in L^\infty(\Omega)$ has been uniformly positive, whereas $\beta \geq 0$ only for models in the time domain. In the frequency domain β turns out to be uniformly negative. In this case γ is an imaginary constant, otherwise $\gamma \geq 0$. Anyway, the chief message of the above discussion is that the proper discretization and efficient solution of problem (17) is a core task in the numerical simulation of electromagnetic fields.

3 Finite element discretization

For the discretization of the variational problem (17) we rely on $\boldsymbol{H}_{\Gamma_D}(\mathbf{curl};\Omega)$–conforming finite element schemes. In order to construct the finite element spaces we first equip the computational domain Ω with a tetrahedral and/or hexahedral triangulation $\mathcal{T}_h$ consisting of elements T_i, $i = 1,\ldots,N_h$. Curved elements are not ruled out, but, as usual, we demand that the elements are uniformly shape regular in the sense of [36], i.e., they must not be severely distorted. Moreover, the Dirichlet part Γ_D of the boundary is assumed to be the union of complete faces of elements.

A vectorfield that is piecewise smooth with respect to $\mathcal{T}_h$ belongs to $\boldsymbol{H}(\mathbf{curl};\Omega)$, if and only if its tangential components across interior faces are continuous [78]. This is a natural requirement for an approximation of the electric field $\boldsymbol{E}$, which sports exactly the same continuity properties. Yet, it takes a judicious choice of local polynomial spaces and degrees of freedom to ensure those conformity conditions.

The credit for introducing $\boldsymbol{H}(\mathbf{curl};\Omega)$–conforming finite element schemes into numerical simulation goes to Nédélec [78, 79], though similar devices had been invented earlier for theoretical purposes [94]. The latter work pursued the construction of discrete differential forms, a perspective that proves particularly rewarding [23, 26, 27]. To appreciate this, recall that Maxwell's equations allow for a very concise formulation in the calculus of differential forms [6], with the electric field being related to 1–forms. It turns out that the point of view of discrete differential forms offers a rather simple and elegant description of the finite element schemes [53].

Two main classes of finite elements in $\boldsymbol{H}(\mathbf{curl};\Omega)$ are known, Nédélec's elements of the first kind [78] ("type–I") and those of the second kind [79] ("type–II"). For the former, the local representation on a tetrahedron T looks like

$$\boldsymbol{\mathcal{NP}}_k(T) := (\mathcal{P}_{k-1}(T))^3 + \left\{\boldsymbol{p} \in (\mathcal{P}_k(T))^3\,;\ \langle \boldsymbol{p}(\boldsymbol{x}), \boldsymbol{x}\rangle = 0,\ \forall \boldsymbol{x} \in T\right\}\ ,$$

where $k \in \mathbb{N}$ denotes the polynomial order of the ansatz. The symbol $\mathcal{P}_k(T)$ refers to the space of polynomials of degree $\leq k$ over T. For the lowest order case $k = 1$ this leads to the representation $\boldsymbol{\mathcal{NP}}_1(T) = \{\boldsymbol{x} \mapsto \boldsymbol{a} + \boldsymbol{b} \times \boldsymbol{x},\ \boldsymbol{a}, \boldsymbol{b} \in \mathbb{R}^3\}$. On a hexahedron T aligned with the coordinate axes the local finite element spaces read

$$\boldsymbol{\mathcal{NP}}_k(T) := Q_{k-1,k,k}(T) \times Q_{k,k-1,k}(T) \times Q_{k,k,k-1}(T)\ ,$$

where $Q_{k_1,k_2,k_3}(T)$ is the space of polynomials of degree $\leq k_i$ in the ith coordinate direction, $i = 1, 2, 3$.

In contrast to these incomplete local spaces, Nédélec's elements of the second kind employ full polynomial spaces to approximate each component of the field locally: This means that

$$\boldsymbol{\mathcal{NP}}_k(T) = (\mathcal{P}_k(T))^3 \quad \text{and} \quad \boldsymbol{\mathcal{NP}}_k(T) = (Q_{k,k,k}(T))^3\ ,$$

for a tetrahedron and hexahedron, respectively.

The global degrees of freedom must both supply a unique characterization of a finite element function and ensure that the appropriate matching conditions at interelement boundaries are satisfied. Please note that point evaluations — suitable degrees of freedom for $H^1(\Omega)$–conforming finite elements — are pointless for want of global continuity; on spaces of 1–forms, with which we are dealing, path integrals are the natural functionals. Thus, in the lowest order case $k = 1$, we pick (weighted) path integrals along edges of elements as degrees of freedom: For lowest order Nédélec–elements of the first kind built upon a mesh $\mathcal{T}_h$ the degrees of freedom are defined by

$$\boldsymbol{\xi} \mapsto \int_e \langle \boldsymbol{\xi}(s), \boldsymbol{t}\rangle\ d\Gamma(s)\,, \quad e \text{ edge of } \mathcal{T}_h\ . \tag{18}$$

Here $\boldsymbol{t}$ stands for the unit tangential vector along e. Please note that the edges have to be endowed with an orientation before an evaluation of (18). Additional first moments of path integrals along edges are introduced as degrees of freedom for type–II elements.

The form of the degrees of freedom accounts for the widely used term "edge elements" coined for $\boldsymbol{H}(\mathbf{curl};\Omega)$–conforming finite element schemes. In higher order cases

further moments of tangential components on edges and faces as well as moments over the whole element occur as degrees of freedom [49, 78].

It can be shown [53, 78] that the degrees of freedom associated with a face completely determine the tangential components of the finite element vectorfield on that face. Hence, global $\boldsymbol{H}(\mathbf{curl};\Omega)$–conformity is guaranteed and the construction of the global finite element spaces is accomplished. We adopt the notation $\boldsymbol{\mathcal{ND}}_k(\mathcal{T}_h)$ for an edge element space of polynomial order k and of either kind based on the triangulation $\mathcal{T}_h$.

Dirichlet boundary conditions are easily incorporated by just the values of degrees of freedom associated with edges on Γ_D. Thus we get the finite element subspace $\boldsymbol{\mathcal{ND}}_{k,\Gamma_D}(\mathcal{T}_h)$ of $\boldsymbol{H}_{\Gamma_D}(\mathbf{curl};\Omega)$. In the lowest order case its dimension evidently equals the number $N_{e,h}$ of edges of $\mathcal{T}_h$ not contained in the closure of Γ_D (for type–I) or twice that number (for type–II).

The edge element spaces should not be branded "exotic" [72], since they feature all desirable properties of standard finite element spaces:

To begin with, they possess locally supported basis functions at worst confined to the union of elements sharing an edge. Moreover, these basis functions have simple representations. For simplicial meshes the formulas are based on the barycentric coordinate functions [99]. As the entries of the $N_{e,h} \times N_{e,h}$ stiffness matrix $\mathbb{A}_h$ related to (17) arise from plugging these nodal basis functions into the bilinear form $a(\cdot,\cdot)$, their computation is straightforward. Also, it is clear that $\mathbb{A}_h$ displays the customary pronounced sparsity of finite element matrices.

Secondly, edge elements form affine families of finite elements (cf. [36]), since the local spaces can be obtained from a polynomial space defined on reference elements through an invertible transformation that leaves the values degrees of freedom unaffected. This particular transformation is the following covariant mapping of vectorfields [78]

$$\boldsymbol{\xi}_h(\boldsymbol{x}) = D\Phi^T(\boldsymbol{x})(\widehat{\boldsymbol{\xi}}_h \circ \Phi)(\boldsymbol{x}) \quad \boldsymbol{x} \in T \;, \tag{19}$$

where $\Phi : T \mapsto \widehat{T}$ is a diffeomorphic mapping of the element T onto the reference element $\widehat{T}$. This offers a second option for the efficient assembly of $\mathbb{A}_h$ via transformation formulas. Furthermore, thanks to affine equivalence, isoparametric edge elements are readily available, implicitly defined by the mapping Φ.

Thirdly, the approximation properties of edge element spaces are as good as one can expect of a scheme whose local spaces comprise all polynomials of a certain degree. More precisely, if a quasiuniform triangulation of meshwidth h is assumed, we get for type–I edge elements of order k and $0 \le s \le m \le k$

$$\begin{aligned}
\inf_{\boldsymbol{\eta}_h \in \boldsymbol{\mathcal{ND}}_k(\mathcal{T}_h)} \|\boldsymbol{U} - \boldsymbol{\xi}_h\|_{H^s(\Omega)} &\le Ch^{m-s}\|\boldsymbol{U}\|_{H^m(\Omega)} \;, && \boldsymbol{U} \in H^m(\Omega) \\
\inf_{\boldsymbol{\eta}_h \in \boldsymbol{\mathcal{ND}}_k(\mathcal{T}_h)} \|\mathbf{curl}(\boldsymbol{U} - \boldsymbol{\xi}_h)\|_{H^s(\Omega)} &\le Ch^{m-s}\|\mathbf{curl}\,\boldsymbol{U}\|_{H^m(\Omega)} \;, && \mathbf{curl}\,\boldsymbol{U} \in H^m(\Omega) \;.
\end{aligned} \tag{20}$$

Applying Cea's lemma [36], we immediately arrive at a priori error estimates for the discrete variational problem (17) in the positive definite case. A more detailed investigation of the approximation properties of edge elements for various problems arising from Maxwell's equations can be found in [71, 72]. In [67, 81] the error introduced

by discretization in time is taken into account, as well. An analysis of the p–version of edge element schemes is carried out in [73]. Numerical dispersion occurring when approximation the vector wave equation by means of edge elements is investigated in [75]. [74] studies superconvergence that has been observed on regular hexahedral grids. [26] deals with coupling edge elements and boundary elements. Edge elements have also been combined with $\boldsymbol{H}(\mathrm{div};\Omega)$–conforming "face elements" to discretize the first order equations (1) and (2) [66].

Apart from these "normal" features, edge elements are exceptional concerning the existence of discrete potentials: For the continuous case it is well known that irrotational vectorfields on simply connected domains can be represented as gradients of scalar potentials (see [49, Thm. 2.9]). This entirely carries over to the discrete setting (see [53, Thm. 20]).

THEOREM 3.1 (Discrete potentials). *For simply connected Ω and Γ_D being a simply connected part of the boundary $\partial\Omega$ we have for type–I edge elements and all $k \geq 1$*

$$\boldsymbol{\mathcal{ND}}_{k,\Gamma_D}(\mathcal{T}_h) \cap \boldsymbol{H}^0(\mathbf{curl};\Omega) = \mathbf{grad}\,\mathcal{S}_{k,\Gamma_D}(\mathcal{T}_h) \;,$$

where $\mathcal{S}_{k,\Gamma_D}(\mathcal{T}_h) \subset H^1_{\Gamma_D}(\Omega)$ denotes the space of Lagrangian finite elements of degree k vanishing on Γ_D.

On topologically more complex domains the assertion of the theorem has to be altered into

$$\boldsymbol{\mathcal{ND}}_{k,\Gamma_D}(\mathcal{T}_h) \cap \boldsymbol{H}^0(\mathbf{curl};\Omega) = \mathbf{grad}\,\mathcal{S}_{k,\Gamma_D}(\mathcal{T}_h) \oplus \mathcal{O}(\mathcal{T}_h) \;, \tag{21}$$

where $\mathcal{O}(\mathcal{T}_h)$ is some space of small dimension, which can be chosen to be $L^2(\Omega)$–orthogonal to $\mathbf{grad}\,\mathcal{S}_{k,\Gamma_D}(\mathcal{T}_h)$. Based on Thm. 3.1, the representation (21) can be established by means of a cutting plane technique applied to the mesh $\mathcal{T}_h$. A closer scrutiny reveals that $\dim\mathcal{O}(\mathcal{T}_h)$ is a topological invariant [48]. We have demanded that $\mathcal{T}_h$ resolves the topological features of Ω. As a consequence, the dimension of $\mathcal{O}(\mathcal{T}_h)$ is independent of the actual mesh.

The gist of Thm. 3.1 is that scalar potentials of **curl**–free vectorfields from Nédélec's spaces are proper finite element functions themselves. In other words, discrete potentials are always *computationally available*. This is a unique trait of edge elements, which is deeply rooted in their close relationship with 1–forms. Of course, for any other $\boldsymbol{H}(\mathbf{curl};\Omega)$–conforming finite element space the mere existence of scalar potentials is guaranteed. However, they remain elusive, as, except under very special circumstances, no convenient finite element representation can be found.

Since edge elements were suggested there has been a debate on why they should be preferred to approximating each component of the electric field by means of classical Lagrangian ("nodal") finite elements. This alternative approach already yielded second order accuracy in the simplest case and seamlessly fits traditional codes. Since we firmly champion edge elements, we want to present the main reasons in their favor:

1. Edge elements are hardly more costly computationally than nodal elements. This is obvious for hexahedral grids and on tetrahedral meshes enhanced sparsity of the matrix offsets the slightly increased number of unknowns [25].

2. Boundary conditions for tangential components can easily be implemented for edge elements, as explained above. Conversely, nodal elements run into difficulties when confronted with edges and corners of $\partial\Omega$.

3. In the presence of reentrant edges, there might be solutions of (17) that cannot be approximated by nodal finite elements at all. As shown in [39], $(H^1(\Omega))^3$ is a genuine closed subspace of $\boldsymbol{H}_0(\mathbf{curl};\Omega) \cap \boldsymbol{H}(\mathrm{div};\Omega)$ in this case. Thus, the only way to get an accurate solution is to use edge elements, unless one supplements the nodal finite element space with particular singular solutions [21] or relaxes continuity requirements [82]. Moreover, if unphysical total continuity of the electric fields at material boundaries is enforced, the consistency of the approximation is destroyed [25].

4. Concerning eigenvalue computations for the $\mathbf{curl}\,\mathbf{curl}$–operator, it is well known that approximations based on $H^1(\Omega)$–conforming finite elements are haunted by "spurious modes" [25]. Though not fully understood, this phenomenon hints at a profound instability of nodal elements. Edge elements help to avoid these and perform superbly on any kind of mesh [20].

5. As will become clear in this paper, the existence of potentials in a simple finite element space is the key to the construction of highly efficient adaptive multilevel schemes for the variational problem (17). Only edge elements meet this requirement unconditionally.

Remark. We point out that there is a close link between the hugely popular Yee's finite difference scheme [76, 98] and the finite integration technique, respectively, and edge elements on hexahedral grids. The connection is established by considering a lumped method, which relies on the second order accurate quadrature rule based on the vertices of the elements. Applying it to evaluate the entries of the stiffness matrix for (17) in the case of constant coefficients, we get the same matrix as for the above mentioned discretization schemes [72].

4 Helmholtz–decompositions

A field where adaptive multilevel techniques have been applied with tremendous success is the numerical solution of elliptic boundary value problems. It is their very feature of ellipticity that makes these problems particularly amenable to the above mentioned type of schemes.

In an intuitive sense, ellipticity of a linear differential operator means that when applied to harmonics it effects an amplification that is a monotonically increasing function of the frequency only. Crudely speaking, this implies a virtual decoupling of smooth and oscillatory functions.

In a formal sense, for a linear second order differential operator L with associated bilinear form $l(\cdot,\cdot) : V \times V \mapsto \mathbb{R}$, $V \subset H^1(\Omega)$, ellipticity is distinguished by the estimate

$$|l(u,u)| \geq \underline{\alpha}\, \|u\|^2_{H^1(\Omega)} \quad \forall u \in V \tag{22}$$

for some constant $\underline{\alpha} > 0$. This means that L behaves like the Laplacian Δ when acting on oscillatory functions.

What about the ellipticity of the operator A related to the bilinear form $a(\cdot,\cdot)$ from (17)? Let us temporarily consider the positive definite case and, in particular, consider $\alpha \equiv 1$, $\beta \equiv 1$, and $\gamma \equiv 0$. Then, in the sense of distributions we get

$$A = \mathbf{curl}\,\mathbf{curl} + Id\ .$$

Obviously, A agrees with the identity mapping on the null space $\boldsymbol{H}^0(\mathbf{curl};\Omega)$ of the **curl**–operator. As $\boldsymbol{H}^0(\mathbf{curl};\Omega)$ contains any gradient, it is teeming with oscillatory functions, whose H^1–norms can be arbitrarily large compared to their L^2–norms. This spells a blatant violation of (22).

However, taking into account that for sufficiently smooth vectorfields

$$A = -\Delta + \mathbf{grad}\,\mathrm{div} + Id\ ,$$

we see that the Laplacian is actually hidden in A; it emerges, once we restrict A to divergence–free vectorfields. Those are characterized as being orthogonal to any gradient in $\mathbf{grad}\, H^1_0(\Omega)$. Now, recall that these gradients form the bulk of $\boldsymbol{H}^0(\mathbf{curl};\Omega)$. In particular, since $\mathbf{grad}\, H^1_{\Gamma_D}(\Omega) \subset \boldsymbol{H}^0_{\Gamma_D}(\mathbf{curl};\Omega)$ we may tersely write

$$A = -\Delta + Id \quad \text{on} \quad \boldsymbol{H}^{\perp}_{\Gamma_D}(\mathbf{curl};\Omega)\ , \tag{23}$$

where we adopted the notation $\boldsymbol{H}^{\perp}_{\Gamma_D}(\mathbf{curl};\Omega)$ for the orthogonal complement of the nullspace of **curl** in $\boldsymbol{H}_{\Gamma_D}(\mathbf{curl};\Omega)$. Thus, we recover ellipticity in a strict sense on $\boldsymbol{H}^{\perp}_{\Gamma_D}(\mathbf{curl};\Omega)$. To put it rigorously, one can prove [49, Thm. 3.9] that on convex domains $\boldsymbol{H}^{\perp}_{\partial\Omega}(\mathbf{curl};\Omega) \subset \boldsymbol{H}^1(\Omega)$ and for an $\underline{\alpha} > 0$

$$|a(\boldsymbol{\eta},\boldsymbol{\eta})| \geq \underline{\alpha}\, \|\boldsymbol{\eta}\|^2_{\boldsymbol{H}^1(\Omega)} \quad \forall \boldsymbol{\eta} \in \boldsymbol{H}^{\perp}_{\partial\Omega}(\mathbf{curl};\Omega)\ .$$

With the $H^{1/2}(\Omega)$–norm instead of the $H^1(\Omega)$–norm, this result is valid for general Lipschitz–domains [3, Thm. 2.17].

It remains to deal with the nullspace of the **curl**–operator. In order to obtain an elliptic problem, we exploit potentials: First it is immediate that ($*$ tags the adjoint of an operator)

$$\mathbf{grad}^* \circ A \circ \mathbf{grad} = \Delta \quad \text{in} \quad H^1_{\Gamma_D}(\Omega)\ . \tag{24}$$

In general, we have $\boldsymbol{H}^0_{\Gamma_D}(\mathbf{curl};\Omega) = \mathbf{grad}\, H^1_{\Gamma_D}(\Omega) + \mathcal{O}(\Omega)$ with $\dim \mathcal{O}(\Omega) \ll \infty$. Ignoring the "small" space $\mathcal{O}(\Omega)$ for the moment, (24) instantly cures the lack of ellipticity on the nullspace of the **curl**–operator.

These considerations illustrate that we can arrive at neat second order elliptic problems by treating the two components of the $a(\cdot,\cdot)$–orthogonal splitting

$$\boldsymbol{H}_{\Gamma_D}(\mathbf{curl};\Omega) = \boldsymbol{H}^0_{\Gamma_D}(\mathbf{curl};\Omega) \oplus \boldsymbol{H}^{\perp}_{\Gamma_D}(\mathbf{curl};\Omega) \tag{25}$$

separately. In a slight generalization of the term, we refer to (25) as the *Helmholtz–decomposition* of the function space. It is a powerful device in the analysis of numerical schemes for Maxwell's equations [67, 71, 81].

So far, we have stuck to the continuous setting. In principle, the arguments elaborated above, remain valid for the discrete problem. This is immediate, as far as the nullspace of the **curl**–operator is concerned: Thanks to the representation theorem 3.1, the lifting (24) whisks us into a very handy finite element space: For lowest order type–I edge elements, we get

$$\mathbf{grad}^* \circ A_h \circ \mathbf{grad} = \Delta_h \ , \tag{26}$$

where Δ_h agrees with the discrete Laplacian generated by piecewise linear, continuous finite elements $\mathcal{S}_{1,\Gamma_D}(\mathcal{T}_h)$. Again, we stress that without simple discrete potentials, Δ_h in (26) would correspond to the Laplacian in some awkward piecewise polynomial space which not necessarily is a proper finite element space at all.

Issues concerning the orthogonal complement are more disturbing, as the discrete orthogonal complement $\boldsymbol{\mathcal{ND}}^{\perp}_{1,\Gamma_D}(\Omega)$ of $\boldsymbol{\mathcal{ND}}^{0}_{1,\Gamma_D}(\Omega)$ itself is utterly inaccessible. We just point out that no locally supported basis of $\boldsymbol{\mathcal{ND}}^{\perp}_{1,\Gamma_D}(\Omega)$ is available. Even worse, computing functions in this orthogonal complement is prohibitively expensive. Similarly daunting is the fact that $\boldsymbol{\mathcal{ND}}^{\perp}_{1,\Gamma_D}(\Omega) \not\subset \boldsymbol{H}^{\perp}_{\Gamma_D}(\mathbf{curl};\Omega)$ which thwarts (23) in the discrete setting.

Yet, our objective are algorithms whose very soul is the idea to approximate the inverse of the discrete operator A_h and to do so uniformly well, no matter what the meshwidth is. Thus, exact orthogonality should not be quintessential; functions $\boldsymbol{\tau}_h \in \boldsymbol{\mathcal{ND}}_{1,\Gamma_D}(\Omega)$ that are "sufficiently" orthogonal to the nullspace will do. All we have to make sure is that the angle between $\boldsymbol{\tau}_h$ and $\boldsymbol{\mathcal{ND}}^{0}_{1,\Gamma_D}(\Omega)$ is bounded from below independently of h.

What are promising candidates for such functions? It turns out that we can simply rely on the nodal basis functions. A crucial clue is offered by the estimate

$$\|\boldsymbol{\xi}_e\|_{0;\Omega} \leq C h_e \, \|\mathbf{curl}\, \boldsymbol{\xi}_e\|_{0;\Omega} \ , \tag{27}$$

where $\boldsymbol{\xi}_e$ is the edge element basis function belonging to the edge e, $h_e \approx \operatorname{diam}\operatorname{supp}(\boldsymbol{\xi}_e)$, and $C > 0$ is a constant that can be chosen independently of e. The estimate (27) implies that for a quasiuniform mesh with meshwidth h the angle $\angle(\boldsymbol{\xi}_e, \boldsymbol{\mathcal{ND}}^{0}_{1,\Gamma_D}(\Omega)) \to \pi/2 + O(h)$. The bottom line is that on fine meshes the nodal basis functions are very close to $\boldsymbol{\mathcal{ND}}^{\perp}_{1,\Gamma_D}(\Omega)$.

5 Adaptive grid refinement

Our ultimate objective is to compute an approximate finite element solution of the continuous variational problem matching a prescribed accuracy with minimal computational effort. A decisive part of this endeavor is the construction of "optimal" triangulations, providing a desired accuracy of the finite element solution with as little elements as possible. Of course, there are many ways to measure the quality of a discrete solution. We will rely on global integral norms for this purpose, in particular the *energy norm* $\|\cdot\|_A$ induced by the bilinear form $a(\cdot,\cdot)$ in the s.p.d. case. Then, a solution $\boldsymbol{E}_h$ passes as acceptable, if the energy norm of the error $\boldsymbol{\chi} := \boldsymbol{E} - \boldsymbol{E}_h$ is below a fixed tolerance τ.

Usually, electromagnetic fields display pronounced *local features*, e.g., singularities at material interfaces. To maintain the overall accuracy of the finite element solution without wasting computer resources, *locally refined meshes* are indispensable. Of course, a nearly optimal mesh cannot be constructed all at once, but has to be built through a process of gradual improvement:

Given a mesh $\mathcal{T}_H$ and a related solution $\boldsymbol{E}_H$ of the discrete variational problem, we need an element–oriented *local a–posteriori estimate* η_T of the norm of the error on each element $T \in \mathcal{T}_H$, i.e. $\eta_T \approx \|\boldsymbol{\chi}\|_{A;T}$. Obviously, summing up the squares of the local quantities η_T supplies an estimate for the norm $\|\chi\|_A^2$ of the global error. If $\|\chi\|_A^2 < \tau^2$, we can quit the process.

Otherwise, elements for which $\eta_T^2 \geq \sigma\, \xi_{\text{tol}}$ (σ is a safety factor in $]0;1[$) are marked for refinement. Popular strategies to obtain the threshold ξ_{tol} are the maximum, the mean value or the more complicate extrapolation strategy. In the case of the mean value strategy the threshold value is defined by

$$\xi_{\text{tol}} := \frac{1}{n_H} \sum_{T \in \mathcal{T}_H} \eta_T^2$$

and the safety factor σ is chosen as ≈ 0.95. Here, n_H is the number of elements of the triangulation $\mathcal{T}_H$. The common idea behind these strategies is to strive for an *equidistribution* of the error. Please note that we owe the possibility to combat large errors in small regions by local refinement at those very sites to the ellipticity of the problem.

Now, the issue is how to refine a marked element. For hexahedral elements this is easily achieved by cutting it into two, four, or eight parts. The situation is more involved for tetrahedral meshes. In this case, we may resort to the bisection algorithm of Bänsch [5], extending the 2D concepts of Bank et al. [7], which divides each marked element into two subelements. We may also use the refinement techniques proposed by Bey [16], where each marked element will be decomposed into eight subelements. Then, special precautions can be taken to avoid "hanging nodes", but those can easily be dealt with by plain interpolation of the finite element functions. Both strategies guarantee that the shape regularity of the triangulation is inherited by the new mesh. Moreover, they lead to *nested meshes* $\mathcal{T}_H \prec \mathcal{T}_h$, for which each element of $\mathcal{T}_H$ is the union of elements of $\mathcal{T}_h$.

Once the refined mesh $\mathcal{T}_h$ is available, we can assemble and solve the related linear system of equations. This yields a presumably improved discrete solution $\boldsymbol{E}_h$ and another cycle of adaptive refinement can be carried out. Eventually, we end up with a sequence $\mathcal{T}_0 \prec \mathcal{T}_1 \prec \ldots \prec \mathcal{T}_L$, $L \in \mathbb{N}$, of nested meshes.

Despite adaptive refinement, a reasonably accurate discrete solution of a three–dimensional problem may still require scores of degrees of freedom, which rules out using direct solvers, except, perhaps, on $\mathcal{T}_0$. Instead iterative solution methods should be used for the large sparse linear systems. Besides, by interpolating the approximate solution from $\mathcal{T}_{l-1}$ onto $\mathcal{T}_l$ we can get a good initial guess. This *nested iteration strategy* [51, Ch. 5] finally tips the balance in favor of iterative schemes.

However, we have to control the inevitable iteration error. The most plausible approach is to demand that the norm of the iteration error should be smaller than 2^{-p} times the estimated error norm on the previous level. This appears reasonable for

a scheme of approximation order p in the energy norm; lowest order edge elements are a first order scheme. Of course, a generous security margin, introduced by some security factor ρ, $0 < \rho \ll 1$ is advisable. Strictly speaking, the iteration error enters the estimate for $\|\chi\|_A$. Yet in the remainder of the paper, we will neglect it.

6 A posteriori error estimation

Ideally, an a–posteriori error estimator should match three conditions which are in general conflicting:

1. It should be *local*: The estimator can be written as the sum of local contributions, and the computation of the local contribution η_T for an element T must be cheap in the sense that it relies on only a fixed small number of nodal values of the approximate solution.

2. It should be *reliable*: This means that the estimate η for $\|\chi\|_A$ satisfies $\|\chi\|_A \leq C\,\eta$ with a constant independent of the mesh. This property ensures that very inaccurate solution are not accepted.

3. It should be *efficient*: $\|\chi\|_{A;D_T} \geq C\,\eta_T$, where $C > 0$ must not depend on the mesh. Here, $\|\cdot\|_{A;D_T}$ denotes the energy norm restricted on a small neighborhood of T. Then, unnecessary refinement is suppressed.

Sometimes it is also interesting to obtain an error estimator which is asymptotically exact, i.e., the ratio between true and estimated error tends to one with an increasing number of refinement steps. Such an error estimator guarantees that a given accuracy can be reached within the adaptive multilevel algorithm using an almost minimal number of unknowns.

For the sake of simplicity, we restrict ourselves to the lowest order case, $k = 1$, of Nédélec–elements of the first kind and to $\Gamma_D = \partial\Omega$. In addition, the existence of discrete potentials is assumed for all irrotational edge element vectorfields. Yet, our results can be easily extended to more general situations, higher order elements or elements of the second kind. As for the space $\mathcal{O}(\mathcal{T}_h)$, it can safely be ignored for the purpose of a–posteriori error estimation, since a basis of this space is always contained in the finite element space. This will be discussed in greater detail in subsection 7.1 in a different context. Further, we only consider cases where β is uniformly positive.

The semidefinite case can be easily included by ignoring information about the irrotational components of the error in regions where $\beta = 0$. The fully indefinite case, where $\beta < 0$ defies a rigorous theoretical treatment, as we do not have a "natural" energy norm induced by the bilinear from $a(\cdot,\cdot)$ at our disposal. However, the techniques presented below may still be applied successfully, if the ratio $|\beta|/\alpha$ is moderate. A more quantitative analysis will be postponed to subsection 7.4. Anyway, under these circumstances we can still use the local contributions η_T to control the refinement process, though reliability and efficiency is no longer guaranteed. To hint at these shortcomings, the term *error indicator* has been introduced.

In the spirit of Sect. 4, we aim to draw on firmly established concepts for a–posteriori error estimators for second order elliptic problems. Naturally, the Helmholtz–decomposition of the function space comes into play, which gives rise to an

$a(\cdot,\cdot)$–orthogonal decomposition of the error $\boldsymbol{\chi} := \boldsymbol{E} - \boldsymbol{E}_h$, where $\boldsymbol{E} \in \boldsymbol{H}_{\partial\Omega}(\mathbf{curl};\Omega)$ and $\boldsymbol{E}_h \in \boldsymbol{\mathcal{ND}}_{1,\partial\Omega}(\mathcal{T}_h)$ are the continuous and discrete solutions of (17), respectively:

$$\boldsymbol{\chi} = \boldsymbol{\chi}^0 + \boldsymbol{\chi}^\perp, \quad \boldsymbol{\chi}^0 \in \boldsymbol{H}^0_{\partial\Omega}(\mathbf{curl};\Omega),\ \boldsymbol{\chi}^\perp \in \boldsymbol{H}^\perp_{\partial\Omega}(\mathbf{curl};\Omega). \tag{28}$$

Thanks to (26) and the existence of discrete potentials in $\mathcal{S}_{1,\partial\Omega}(\mathcal{T}_h)$, well known error estimators for the discrete diffusion operator $\mathrm{div}(\beta\,\mathbf{grad}\,\cdot)$ instantly furnish good estimates for $\|\boldsymbol{\chi}^0\|_A$.

To tackle $\boldsymbol{\chi}^\perp$, we recall that on the weakly solenoidal part of the Helmholtz decomposition the bilinear form $a(\cdot,\cdot)$ is elliptic. This motivates our policy to obtain local estimates for $\boldsymbol{\chi}^\perp$ by means of slightly modified standard strategies. Two of those will be discussed in the following subsections. Several others, like everaging error estimators [10, 102], are not covered in this presentation.

Remark. The idea to use the Helmholtz–decomposition for the design of error estimators is a valuable guideline beyond problems in $\boldsymbol{H}(\mathbf{curl};\Omega)$. Its relevance was first realized for problems in $\boldsymbol{H}(\mathrm{div};\Omega)$ [2, 57].

6.1 Residual based error estimator

This kind of error estimator is based on an appropriate evaluation of the dual norm of the residual as a continuous linear functional. The concept of residual based error estimation has been introduced in an early work of Babuška and Rheinboldt [4] and has been further developed and analyzed by various authors [22, 46, 62, 89, 90]. Originally, introduced for standard conforming discretization schemes for elliptic equations such estimators have been extended within the last few years to nonconforming and mixed discretizations, as well as nonlinear applications and parabolic problems see e.g. [2, 34, 47, 56, 57, 59, 60, 62, 96]. For a more general approach concerning error estimators based on dual norms, we refer to [13, 14, 45].

The starting point is the continuous defect problem

$$a(\boldsymbol{\chi},\boldsymbol{\eta}) = r(\boldsymbol{\eta}) := f(\boldsymbol{\eta}) - a(\boldsymbol{E}_h,\boldsymbol{\eta}), \quad \forall \boldsymbol{\eta} \in \boldsymbol{H}_{\partial\Omega}(\mathbf{curl};\Omega). \tag{29}$$

Here, the residual r depends only on the right hand side f of (17) and the finite element solution $\boldsymbol{E}_h$. By means of the $a(\cdot,\cdot)$–orthogonal splitting (28), (29) can be converted into two separate defect problems on the spaces $\boldsymbol{H}^0_{\partial\Omega}(\mathbf{curl};\Omega)$ and $\boldsymbol{H}^\perp_{\partial\Omega}(\mathbf{curl};\Omega)$, respectively: Find $\boldsymbol{\chi}^0 \in \boldsymbol{H}^0_{\partial\Omega}(\mathbf{curl};\Omega)$ such that

$$\left(\beta\boldsymbol{\chi}^0,\boldsymbol{\eta}^0\right)_{0;\Omega} = f(\boldsymbol{\eta}^0) - \left(\beta\boldsymbol{E}_h,\boldsymbol{\eta}^0\right)_{0;\Omega}, \quad \boldsymbol{\eta}^0 \in \boldsymbol{H}^0_{\partial\Omega}(\mathbf{curl};\Omega) \tag{30}$$

and find $\boldsymbol{\chi}^\perp \in \boldsymbol{H}^\perp_{\partial\Omega}(\mathbf{curl};\Omega)$ such that for all $\boldsymbol{\chi}^\perp \in \boldsymbol{H}^\perp_{\partial\Omega}(\mathbf{curl};\Omega)$

$$\left(\alpha\,\mathbf{curl}\,\boldsymbol{\chi}^\perp,\mathbf{curl}\,\boldsymbol{\eta}^\perp\right)_{0;\Omega} + \left(\beta\boldsymbol{\chi}^\perp,\boldsymbol{\eta}^\perp\right)_{0;\Omega} = f(\boldsymbol{\eta}^\perp) - a(\boldsymbol{E}_h,\boldsymbol{\eta}^\perp)\,. \tag{31}$$

According to this splitting the local contributions η_T of the error estimator will be given by $\eta_T^2 = (\eta_T^0)^2 + (\eta_T^\perp)^2$. Here, η_T^0 and $\eta_T^\perp$ are the local contributions of η^0 and $\eta^\perp$ which will yield upper and lower bounds for $\|\boldsymbol{\chi}^0\|_A$ and $\left\|\boldsymbol{\chi}^\perp\right\|_A$, respectively.

Exploiting representations through potentials in $H^1_{\partial\Omega}(\Omega)$ to deal with (30) we end up with the same variational problem as for a standard diffusion equation: We set $\boldsymbol{\chi}^0 = \mathbf{grad}\,\Phi$ where $\Phi \in H^1_{\partial\Omega}(\Omega)$ satisfies

$$(\beta\,\mathbf{grad}\,\Phi, \mathbf{grad}\,\psi)_{0;\Omega} = f(\mathbf{grad}\,\psi) - (\beta \boldsymbol{E}_h, \mathbf{grad}\,\psi)_{0;\Omega}\,, \quad \psi \in H^1_{\partial\Omega}(\Omega). \tag{32}$$

Now, the well–known techniques for the Laplace operator and a standard conforming FE discretization in $\mathcal{S}_{1,\partial\Omega}(\mathcal{T}_h)$ can be applied [90]. For the element $T \in \mathcal{T}_h$ the local contribution η_T^0 to the estimator for the **curl**–free part of the error turns out to be

$$\eta_T^{0\,2} := \frac{h_T^2}{\beta_T}\|\operatorname{div}(\beta\boldsymbol{E}_h - \Pi_1\boldsymbol{f})\|^2_{0;T} + \sum_{F\subset\partial T\cap\Omega} \frac{2h_F\beta_{T_F}}{(\beta_T+\beta_{T_F})^2}\|[\langle \boldsymbol{n}, \beta\boldsymbol{E}_h - \Pi_1\boldsymbol{f}\rangle]_J\|^2_{0;F}\,. \tag{33}$$

Here, $[\cdot]_J$ stands for the jump of a functions across the face F. h_T denotes the diameter of the element $T \in \mathcal{T}_h$ and h_F stands for the diameter of the face F. Π_1 is the projection onto piecewise linear vector fields. The weights β_T and β_{T_F} depend on the coefficient β. They are chosen as the maximum of β restricted on T and T_F, where T_F is the neighbor element of T sharing the face F.

The first part of η_T^0 in (33) is associated with the strong form of the variational problem (32). In the second part the jump of the normal components comes into play. It turns out that the error estimator depends only on the available finite element solution $\boldsymbol{E}_h$ and the right hand side of the original problem. If the coefficients are piecewise constant, we have to compute the corresponding values only in the centers of gravity of the elements and of the edges. Thus, the numerical computation of η_T^0 is very cheap.

Keeping in mind that (31) is a truly elliptic variational problem, we proceed in perfect analogy to the case of a second order elliptic diffusion equation. Since the second order term is associated with the **curl**–operator, we apply Green's formula to $\left(\alpha\,\mathbf{curl}\,\boldsymbol{E}_h, \mathbf{curl}\,\boldsymbol{\eta}^\perp\right)_{0;\Omega}$. As in the standard conforming case, it is then sufficient to use Galerkin orthogonality and an appropriate local quasi–interpolation operator P, which has to satisfy local approximation and stability properties. We may use an analogue of the interpolation operator of Clément [37] or simpler projection operators [80, 85]. This gives us reliability. To confirm efficiency we make use of cubic and quartic bubble functions having a local support and inverse inequalities for polynomials. For a detailed proof we refer to [11].

Eventually, we arrive at the following expression for $\eta_T^\perp$:

$$\eta_T^{\perp\,2} := \min\left(\frac{h_T^2}{\alpha_T}, \frac{1}{\beta_T}\right)\|\,\mathbf{curl}\,\boldsymbol{g}_h + \beta\boldsymbol{E}_h - \Pi_1\boldsymbol{f})\|^2_{0;T} + \\ + \sum_{F\subset\partial T\cap\Omega} \frac{2h_F\alpha_{T_F}}{(\alpha_T+\alpha_{T_F})^2}\|[\boldsymbol{n}\times\boldsymbol{g}_h]_J\|^2_{0;F}\,. \tag{34}$$

The weights correspond to those given for η_T^0 and $\boldsymbol{g}_h := \alpha\,\mathbf{curl}\,\boldsymbol{E}_h$. We recall that in the lowest order case the term $\mathbf{curl}\,\alpha\,\mathbf{curl}\,\boldsymbol{E}_h$ is vanishing for a piecewise constant coefficient α. In contrast to η_T^0, the first term is the norm of a linear function whereas the second is the norm of a constant if the coefficients are piecewise constant. Thus, the norms can be evaluated by using low order quadrature formulas.

Altogether, we obtain the following upper and lower bounds for the error $\boldsymbol{E} - \boldsymbol{E}_h$ in the $\|\cdot\|_A$–norm [11]:

$$c_R\eta - c_{\text{high}}\eta_{\text{high}} \leq \|\boldsymbol{E} - \boldsymbol{E}_h\|_A \leq C_R\eta + C_{\text{high}}\eta_{\text{high}}$$

where in general the term η_{high} is of higher order and can therefore be neglected, if the triangulation is fine enough. We note that for each triangulation there is an example where this term is dominant and the error estimator fails.

6.2 Hierarchical error estimator

Hierarchical basis error estimators are well-known for standard conforming discretizations [8, 40, 43, 90]. They are based on a defect correction in a higher order space and a hierarchical two-level splitting. An excellent overview of different techniques can be found in [22, 90] (see also the references therein).
There are basically two ways to obtain such an error estimator. Using the ideas of Deuflhard, Leinen, Yserentant [40], the resulting continuous defect problem is first discretized and then localized. The second possibility follows Bank and Weiser [8], where the defect problem is first localized and then discretized. These concepts have been generalized to nonconforming discretizations, [58, 95], mixed Raviart-Thomas discretizations, [1, 29, 57, 60] and the Stokes problem [9, 88]. In this section, we present a hierarchical basis error estimator which is based on a defect correction in an appropriate higher order space, a hierarchical splitting, and, finally, localization techniques (cf., e.g., [8, 40, 90].

A characteristic feature of hierarchical estimators is that they are based on saturation assumptions. These assumptions are in general justified to some extend by a priori estimates. We assume that there is a constant $\delta < 1$ independent of $h \leq h_0$ such that the following inequality holds

$$\|\boldsymbol{E} - \boldsymbol{E}_2\|_A \leq \delta_h \|\boldsymbol{E} - \boldsymbol{E}_h\|_A, \tag{35}$$

with $\delta_h \leq \delta < 1$ where $\boldsymbol{E}_2 \in \boldsymbol{\mathcal{ND}}_{2,\partial\Omega}(\mathcal{T}_h)$ is the finite element solution of the variational problem (17) on $\boldsymbol{\mathcal{ND}}_{2,\partial\Omega}(\mathcal{T}_h)$. We recall that (35) always holds with a $\delta \leq 1$. In fact if the solution $\boldsymbol{E}$ is smooth enough, we expect that δ_h tends to zero with decreasing h, i.e., for an increasing number of refinement levels. Under the assumption (35) it is sufficient to consider $\boldsymbol{E}_h - \boldsymbol{E}_2$ to obtain upper and lower bounds for $\|\boldsymbol{E}_h - \boldsymbol{E}\|_A$. In addition, $\boldsymbol{E}_h - \boldsymbol{E}_2$ satisfies the following global discrete defect problem

$$a(\boldsymbol{E}_2 - \boldsymbol{E}_h, \boldsymbol{\eta}) = r(\boldsymbol{\eta}), \quad \boldsymbol{\eta} \in \boldsymbol{\mathcal{ND}}_{2,\partial\Omega}(\mathcal{T}_h) \tag{36}$$

and the residual $r(\cdot)$ is defined as in the previous subsection. Solving (36) is prohibitively expensive. However, for the error estimator it is sufficient to obtain an approximation $\boldsymbol{E}_{\text{err}}$ of $\boldsymbol{E}_2 - \boldsymbol{E}_h$ which has an equivalent $\|\cdot\|_A$–norm and at the same time can be easily computed. A first step towards the definition of $\boldsymbol{E}_{\text{err}}$ is the hierarchical two-level splitting of $\boldsymbol{\mathcal{ND}}_{2,\partial\Omega}(\mathcal{T}_h)$. How this looks like on the element level is depicted in Fig. 1.

Here, $\widetilde{\mathcal{S}}_2(T)$ is the hierarchical surplus of the standard quadratic elements and $\widetilde{\boldsymbol{\mathcal{ND}}}_2^{\perp}(T) := \{\boldsymbol{\xi} \in \boldsymbol{\mathcal{ND}}_2(T) | \ \langle \boldsymbol{\xi}, \boldsymbol{t}_{|e} \rangle = 0, \ e \text{ edge of } T\}$. The Helmholtz–decomposition of the quadratic surplus is conspicuous in this splitting: The irrotational part corresponds to $\widetilde{\boldsymbol{\mathcal{ND}}}_2^{0}(T)$ and $\widetilde{\boldsymbol{\mathcal{ND}}}_2^{\perp}(T)$ is close to the weakly solenoidal

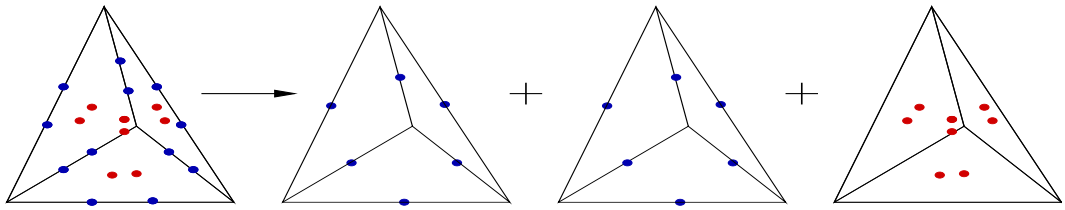

Figure 1: *Degrees of freedom and hierarchical two-level splitting of the local ansatz space.*

component. Note that we have no orthogonality between $\widetilde{\boldsymbol{\mathcal{ND}}}_2^0(T)$ and $\widetilde{\boldsymbol{\mathcal{ND}}}_2^\perp(T)$, since $\boldsymbol{\mathcal{ND}}_{2,\partial\Omega}^\perp(\mathcal{T}_h)$ is not available. Yet the basis functions spanning $\widetilde{\boldsymbol{\mathcal{ND}}}_2^\perp(T)$ are sufficiently orthogonal to the nullspace of the **curl**–operator. Thus, a strengthened Cauchy-Schwarz inequality holds with a constant independent of $T \in \mathcal{T}_h$ and the mesh $\mathcal{T}_h$. The local splitting from Fig. 1 implies the following global decomposition:

$$\boldsymbol{\mathcal{ND}}_{2,\partial\Omega}(\mathcal{T}_h) = \boldsymbol{\mathcal{ND}}_{1,\partial\Omega}(\mathcal{T}_h) \oplus \mathbf{grad}\,\widetilde{\mathcal{S}}_{2,\partial\Omega}(\mathcal{T}_h) \oplus \widetilde{\boldsymbol{\mathcal{ND}}}_{2,\partial\Omega}^\perp(\mathcal{T}_h) \tag{37}$$

where $\widetilde{\mathcal{S}}_{2,\partial\Omega}(\mathcal{T}_h)$ is the global quadratic hierarchical surplus and $\widetilde{\boldsymbol{\mathcal{ND}}}_{2,\partial\Omega}^\perp(\mathcal{T}_h) := \{\boldsymbol{\xi} \in \boldsymbol{\mathcal{ND}}_{2,\partial\Omega}(\mathcal{T}_h) |\ \langle \boldsymbol{\xi}, \boldsymbol{t} \rangle_{|e} = 0,\ e \text{ edge of } \mathcal{T}_h\}$.

Now, we neglect the coupling between the three different global subspaces and replace the bilinear form $a(\boldsymbol{\xi}, \boldsymbol{\chi})$ in (36) by

$$a(\boldsymbol{\xi}_1, \boldsymbol{\chi}_1) + a(\boldsymbol{\xi}_2^0, \boldsymbol{\chi}_2^0) + a(\boldsymbol{\xi}_2^\perp, \boldsymbol{\chi}_2^\perp), \quad \boldsymbol{\xi} = \boldsymbol{\xi}_1 + \boldsymbol{\xi}_2^0 + \boldsymbol{\xi}_2^\perp,\ \boldsymbol{\chi} = \boldsymbol{\chi}_1 + \boldsymbol{\chi}_2^0 + \boldsymbol{\chi}_2^\perp,$$

where $\boldsymbol{\xi}_1,\ \boldsymbol{\chi}_1 \in \boldsymbol{\mathcal{ND}}_{1,\partial\Omega}(\mathcal{T}_h)$, $\boldsymbol{\xi}_2^0,\ \boldsymbol{\chi}_2^0 \in \mathbf{grad}\,\widetilde{\mathcal{S}}_{2,\partial\Omega}(\mathcal{T}_h)$ and $\boldsymbol{\xi}_2^\perp,\ \boldsymbol{\chi}_2^\perp \in \widetilde{\boldsymbol{\mathcal{ND}}}_{2,\partial\Omega}^\perp(\mathcal{T}_h)$. The solution of the modified variational problem is still equivalent to $\boldsymbol{E}_2 - \boldsymbol{E}_h$. This can be proven by a strengthened Cauchy-Schwarz inequality between the three subspaces. In addition, the structure of the modified variational problem is very simple. It turns out that it consists of three independent variational problems. Taking into account the Galerkin orthogonality, we obtain that the solution of the defect problem restricted on the original finite element space $\boldsymbol{\mathcal{ND}}_{1,\partial\Omega}(\mathcal{T}_h)$ is equal to zero. We arrive at the following two remaining variational problems: Find $\Phi \in \widetilde{\mathcal{S}}_{2,\partial\Omega}(\mathcal{T}_h)$ such that

$$(\beta\,\mathbf{grad}\,\Phi, \mathbf{grad}\,\psi)_{0;\Omega} = r(\mathbf{grad}\,\psi), \quad \psi \in \widetilde{\mathcal{S}}_{2,\partial\Omega}(\mathcal{T}_h) \tag{38}$$

and find $\boldsymbol{\Xi}_2^\perp \in \widetilde{\boldsymbol{\mathcal{ND}}}_{2,\partial\Omega}^\perp(\mathcal{T}_h)$ such that

$$a(\boldsymbol{\Xi}_2^\perp, \boldsymbol{\chi}_2^\perp) = r(\boldsymbol{\chi}_2^\perp), \quad \boldsymbol{\chi}_2^\perp \in \widetilde{\boldsymbol{\mathcal{ND}}}_{2,\partial\Omega}^\perp. \tag{39}$$

Then, under the saturation assumption (35), there exist constants $0 < c_{\text{hier}} < C_{\text{hier}}$ independent of the refinement level such that

$$\frac{c_{\text{hier}}}{1+\delta}\left(\|\mathbf{grad}\,\Phi\|_A^2 + \left\|\boldsymbol{\Xi}_2^\perp\right\|_A^2\right)^{1/2} \le \|\boldsymbol{E} - \boldsymbol{E}_h\|_A \le \frac{C_{\text{hier}}}{1-\delta}\left(\|\mathbf{grad}\,\Phi\|_A^2 + \left\|\boldsymbol{\Xi}_2^\perp\right\|_A^2\right)^{1/2}.$$

Both global variational problems (38) and (39) give rise to a stiffness matrix which is spectrally equivalent to its diagonal and its block diagonal matrix where each block is

a 2×2 matrix, respectively. Therefore a further simplification is justified, and we end up with the following definition of the local contribution η_T of the error estimator:

$$\eta_T^2 := \sum_{e \subset \partial T \cap \Omega} \frac{r^2(\mathbf{grad}\, \phi_e)}{n_e a(\mathbf{grad}\, \phi_e, \mathbf{grad}\, \phi_e)} + \frac{1}{2} \sum_{F \subset \partial T \cap \Omega} \|\Xi_F\|_A^2.$$

Here, ϕ_e is the quadratic bubble function associated with the edge e and n_e stands for the number of elements sharing the edge e. Finally, $\Xi_F \in \widetilde{\mathcal{NED}}^{\perp}_{2,\partial\Omega}(F) := \{\boldsymbol{\xi} \in \widetilde{\mathcal{NED}}^{\perp}_{2,\partial\Omega}(\mathcal{T}_h) |\, \boldsymbol{\xi}_{|F'} = 0, F' \neq F\}$ satisfies the two-dimensional variational problem:

$$a(\Xi_F, \boldsymbol{\xi}) = r(\boldsymbol{\xi}), \quad \boldsymbol{\xi} \in \widetilde{\mathcal{NED}}^{\perp}_{2,\partial\Omega}(F).$$

In contrast to the residual based error estimator, we have to solve local low–dimensional subproblems; one 2×2 problem for each face.

Remark. From an algebraic point of view, the error estimator coincides with the correction resulting from a single block Jacobi step applied applied to the discrete defect problem (36) with respect to the hierarchical basis implied by the decomposition (37). The estimate of the error can be improved if we use several block–Gauss–Seidel steps instead of one block–Jacobi step. Although the efficiency index, the ratio between true and estimated error, can be expected to be better, according to our experience, the adaptively generated triangulations will almost be the same.

7 Multigrid method

To make the adaptive approach competitive we urgently need a highly efficient iterative solver for the finite elements equations on fine grids. In this context the notion of "efficiency" implies two essential requirements [51, Ch. 5]:

1. A single step of the iteration should require a computational effort proportional to the number of unknowns.

2. The rate of convergence must be well below 1 and must not deteriorate when the (local) meshwidth becomes very small (asymptotic optimality)

The first criterion is naturally met by most iterative solvers like Gauß–Seidel or CG–variants that rely on purely local computations. Yet single–grid iterative methods, which are by now largely used in commercial software for electromagnetic simulations, inevitably fail on the second criterion (see [52]).

It is now common knowledge that for most *elliptic* problems there is one way to accommodate both requirements: The trick is done by multilevel techniques, with multigrid methods as their most commonplace representative (see [30, 32, 51] and the references therein). To achieve their superior convergence, these methods rely on a hierarchy of refined meshes. Obviously, they perfectly match the adaptive setting, since the required coarse and fine meshes are automatically created during the refinement process. This is another strong incentive to seek to marry the adaptive approach and multigrid methods.

Remark. The performance and robustness of multigrid methods can be enhanced by using them as preconditioner for a Krylov–subspace iterative method like CG. These gains often outweigh the small extra costs. Moreover, the preconditioned CG method (PCG) provides a cheap estimate for the iteration error through the size of the residual.

7.1 Multigrid idea

In recent years a new understanding of multigrid methods for symmetric positive definite variational problems $a(u,v) = f(v)$, $v \in \mathcal{V}$ has emerged (cf. ,e.g., [30, 97, 100]). According to this point of view each step of the iteration boils down to carrying out successive corrections in subspaces V_i, $i \in \{1, \ldots, K\}$ of the finite element space $\mathcal{V}_h \subset \mathcal{V}$ (multiplicative Schwarz method). We get individual corrections $c_i \in \mathcal{V}_i$ of some intermediate approximation as solutions of the defect problems $a(c_i, v_i) = r(v_i)$, $v_i \in \mathcal{V}_i$, where r stands for the current residual. Then one step of the iteration applied to the approximate solution $x_h \in \mathcal{V}_h$ can be described by

$$x_h \leftarrow x_h + c_i\,,\ a(c_i, v_i) = f(v_i) - a(x_h, v_i)\ \forall v_i \in \mathcal{V}_i \quad i = 1, \ldots, K\ .$$

Hence, a multigrid method is fully specified, once the underlying subspace decomposition $V_h = \sum_{i=1}^{K} V_i$ is known. If the dimensions of these subspaces are small, then the computational effort still complies with the first criterion. To confirm that the second condition is fulfilled, we have to establish a kind of uniform stability of the splitting with respect to the energy norm induced by the bilinear form.

What turned out to be a very effective choice for second order elliptic problems discretized by means of standard Lagrangian finite elements, is a *nodal multilevel decomposition* [80]. This refers to a decomposition that, except for the entire finite element space on the coarsest mesh $\mathcal{T}_0$, encompasses only the one–dimensional spaces spanned by the nodal finite element basis functions on all levels of refinement. A closer scrutiny reveals that an ordinary multigrid V–cycle can be recovered as a straightforward successive subspace correction based on this decomposition [97]. The nodal multilevel decomposition can be shown to be actually $H^1(\Omega)$–stable with constants independent of the depth of refinement [30]. In a profound way this property is a consequence of the ellipticity of the operator.

7.2 Multilevel decomposition

Now we focus on the bilinear form $a(\cdot,\cdot)$ from (17) discretized by means of lowest order edge elements of the first kind. In addition, in this section we do not allow negative values of β. To fix the setting, we assume that a sequence of nested triangulations $\mathcal{T}_l$, $l = 0, \ldots, L$, has already been created by repeated adaptive refinement.

To begin with, we know that a plain nodal multilevel decomposition is only suitable for problems of an elliptic character. Thus, a naive multigrid approach to the $\boldsymbol{H}(\mathbf{curl};\Omega)$-elliptic variational problem (17) is doomed: Taking into account the considerations of Sect. 4 it is clear that both parts of the Helmholtz–decomposition have to be taken care of by different splittings.

By and large (26) settles the issue for the irrotational vectorfields, because we can simply copy the successful policy for second order elliptic problems: The conventional

nodal multilevel decomposition of the discrete potential space immediately supplies a the desired splitting of irrotational vectorfields, as far as they possess a representation as gradients. Since $a(\mathbf{grad}\,\psi, \mathbf{grad}\,\phi) = (\beta\,\mathbf{grad}\,\psi, \mathbf{grad}\,\phi)_{0;\Omega}$ the stability estimates for second order elliptic problems remain fully valid for (17).

It remains to deal with $\mathcal{O}(\mathcal{T}_L)$, where the discrete potential space fails. However, in Sect. 3 we learned that $\dim \mathcal{O}(\mathcal{T}_0) = \dim \mathcal{O}(\mathcal{T}_L)$. Elementary linear algebra then proves that $\mathcal{O}(\mathcal{T}_L) \subset \mathbf{grad}\,\mathcal{S}_{1,\Gamma_D}(\mathcal{T}_L) + \mathcal{O}(\mathcal{T}_0)$. Consequently, the coarse grid space $\boldsymbol{\mathcal{ND}}^0_{1,\Gamma_D}(\mathcal{T}_0)$ can already contribute all those odd **curl**–free vectorfields outside $\mathbf{grad}\,\mathcal{S}_{1,\Gamma_D}(\mathcal{T}_L)$. Hence, the final splitting of the irrotational part of the Helmholtz–decomposition reads:

$$\boldsymbol{\mathcal{ND}}^0_{1,\Gamma_D}(\mathcal{T}_L) = \boldsymbol{\mathcal{ND}}^0_{1,\Gamma_D}(\mathcal{T}_0) + \sum_{l=1}^{L} \sum_{\boldsymbol{x}\in\mathcal{V}_l^{\mathrm{new}}} \mathrm{Span}\,\{\mathbf{grad}\,\psi_{\boldsymbol{x}}\} \tag{40}$$

Here, we wrote $\psi_{\boldsymbol{x}}$ for the nodal basis function of $\mathcal{S}_1(\mathcal{T}_l)$ perched on the vertex $\boldsymbol{x}$. The choice of the relevant vertices on level l, which form the set $\mathcal{V}_l^{\mathrm{new}}$, is inspired by the idea of "local multigrid" (see [68]). Putting it tersely, no basis function must occur twice (40). Thus, for big values of l, only nodes in regions where massive adaptive refinement has taken place are incorporated into $\mathcal{V}_l^{\mathrm{new}}$. Unless such a strategy is implemented, overall efficiency might be squandered.

The recipe how to handle the orthogonal complement $\boldsymbol{\mathcal{ND}}^{\perp}_{1,\Gamma_D}(\mathcal{T}_L)$ has already been outlined in Sect. 4. We have seen that we can count on ellipticity in this case and therefore a multilevel nodal decomposition looks promising. As discussed before, there are no locally supported basis functions exactly lying in $\boldsymbol{\mathcal{ND}}^{\perp}_{1,\Gamma_D}(\mathcal{T}_L)$ and we cannot require this for the splitting either. Yet, following the arguments in Sect. 4, a satisfactory approximate splitting can be based on the edge element basis functions. Consequently, we incorporate the one–dimensional spaces, spanned by edge element basis functions on all levels of refinement into the multilevel decomposition. Again, we have to avoid multiple occurrences of the same subspace by applying the "local multigrid" selection criterion specified above: only those edges belong to the set $\mathcal{E}_l^{\mathrm{new}}$ that either have been created in the lth step of refinement or whose associated edge element basis function has changed.

One might object that the sum of all these subspaces is way too large, since it agrees with the total finite element space, whereas the weakly solenoidal vectorfields are no more than a subspace. However, note that in any nodal multilevel splitting there is a massive "overlap" between the subspaces. Indeed, this redundancy accounts for the excellent stability of the splittings [80]. It is rather desirable than worrisome that the splitting extends beyond the targeted subspace.

Ultimately, by merging the splitting for both parts of the Helmholtz decomposition, we arrive at

$$\boldsymbol{\mathcal{ND}}_{1,\Gamma_D}(\mathcal{T}_L) = \boldsymbol{\mathcal{ND}}_{1,\Gamma_D}(\mathcal{T}_0) + \sum_{l=1}^{L} \sum_{e\in\mathcal{E}_l^{\mathrm{new}}} \mathrm{Span}\,\{\boldsymbol{\xi}_e\} + \sum_{l=1}^{L} \sum_{\boldsymbol{x}\in\mathcal{V}_l^{\mathrm{new}}} \mathrm{Span}\,\{\mathbf{grad}\,\psi_{\boldsymbol{x}}\}\ . \tag{41}$$

Thus far, the energetic stability of (41) can only be shown under restrictive assumptions [54]:

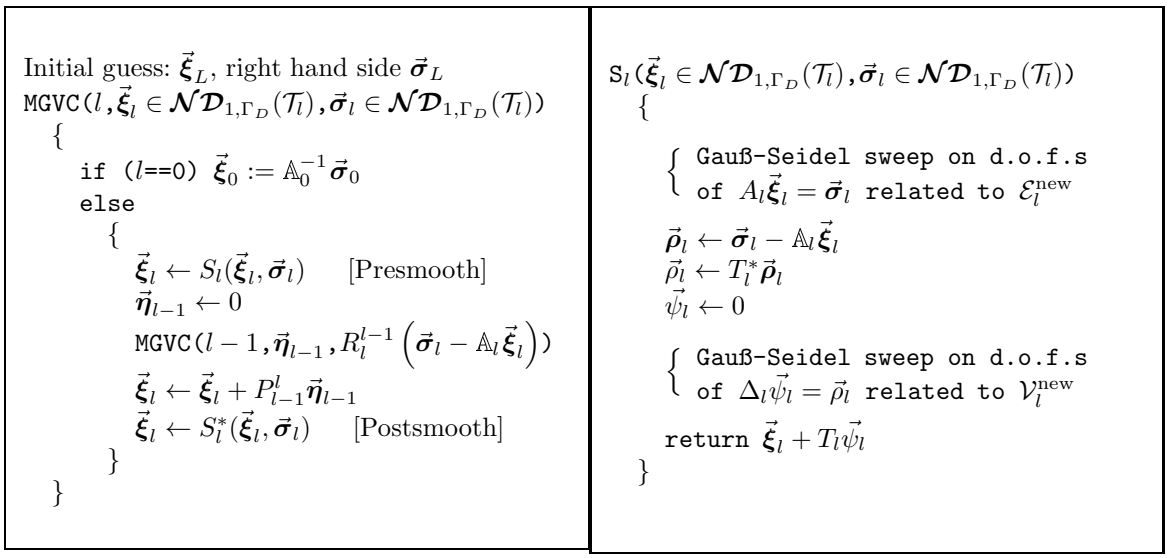

Figure 2: **Left**: *Recursive implementation of multigrid V(1,1)–cycle for the discrete variational problem related to* $a(\cdot,\cdot)$. **Right**: *Evaluation of the hybrid smoother* $S_l(\vec{\xi}_l, \vec{\sigma}_l)$.

THEOREM 7.1. *We assume that* $\Omega \subset \mathbb{R}^3$ *is* convex *and* $\Gamma_D = \partial\Omega$. *If the sequence* $(\mathcal{T}_l)_{l=0}^L$ *of nested meshes has been obtained by* uniform refinement, *then the decomposition (41) of* $\mathcal{NED}_{1,\Gamma_D}(\mathcal{T}_L)$ *is stable with respect to the energy semi–norm induced by* $a(\cdot,\cdot)$ *with constants independent of the depth* L *of refinement.*

However, the size of jumps of the coefficient functions α and β enter the constants as well as their relative scaling.

7.3 Algorithmic aspects

From the algebraic point of view the multigrid algorithm is uniquely determined by the decomposition (41). Yet the subspace corrections have to be implemented in a multigrid fashion to achieve optimum computational complexity. The principal idea is to avoid visiting the finest grid after each correction in the direction of a coarse grid function. Instead the exchange of information between different levels of refinement is effected by evaluating transfer operators (restriction, prolongation) [51]. This gives rise to a multigrid cycle depicted in Fig. 2, left. Symbols with small arrows on top designate coefficient vectors with respect to the canonical bases of the finite element spaces.

The operators $P_{l-1}^l : \mathcal{NED}_{1,\Gamma_D}(\mathcal{T}_{l-1}) \mapsto \mathcal{NED}_{1,\Gamma_D}(\mathcal{T}_l)$ and $R_l^{l-1} : \mathcal{NED}_{1,\Gamma_D}(\mathcal{T}_l) \mapsto \mathcal{NED}_{1,\Gamma_D}(\mathcal{T}_{l-1})$ designate the canonical intergrid transfers, prolongation and restriction, in the Nédélec spaces, induced by the natural embedding of these spaces (see [51]). They are transposes of each other and permit a purely local evaluation.

The distinctive feature of the method is the design of the smoother $S_l(\cdot,\cdot)$, whose steps are described in Fig. 2. It might be dubbed a "hybrid" Gauß–Seidel smoother, since smoothing sweeps both in the space of edge elements and the scalar potential spaces $\mathcal{S}_{1,\Gamma_D}(\mathcal{T}_l)$ are carried out. In Fig. 2 Δ_l stands for the linear operator (i.e. the stiffness matrix) related to the bilinear form $(\phi_l, \psi_l) \mapsto (\beta\,\mathbf{grad}\,\phi_l, \mathbf{grad}\,\psi_l)_{0;\Omega}$ in $\mathcal{S}_{1,\Gamma_D}(\mathcal{T}_l)$. The Gauß–Seidel relaxation of any linear system is invariably supposed to be based on the canonical bases of the finite element spaces.

Let us take a closer look at the smoother S_l applied to $\boldsymbol{\xi}_l$ with right hand side $\boldsymbol{\sigma}_l$. Its evaluation boils down to that part of the successive subspace correction related to level l. Correcting an approximate solution in the direction of some edge element basis functions just amounts to a plain Gauß–Seidel sweep applied to a part of the stiffness matrix $\mathbb{A}_l$.

As for the one–dimensional subspaces spanned by the gradients of basis functions in $\mathcal{S}_{1,\Gamma_D}(\mathcal{T}_l)$, a local correction $\mathbf{grad}\,\gamma_l \in \mathrm{Span}\,\{\mathbf{grad}\,\psi_{\boldsymbol{x}}\}$, $\boldsymbol{x} \in \mathcal{V}_l^{\mathrm{new}}$, of the intermediate solution $\widetilde{\boldsymbol{\xi}}_l$ is obtained from

$$a(\mathbf{grad}\,\gamma_l, \mathbf{grad}\,\psi_{\boldsymbol{x}}) = \left(\boldsymbol{\sigma}_l - A_l\widetilde{\boldsymbol{\xi}}_l, \mathbf{grad}\,\psi_{\boldsymbol{x}}\right)_{0;\Omega} \ .$$

Actually, this is a scalar equation, whose right hand side is calculated by evaluating the residual, which is a linear form on $\boldsymbol{\mathcal{ND}}_{1,\Gamma_D}(\mathcal{T}_l)$, for the argument vector $\mathbf{grad}\,\boldsymbol{\psi}_{\boldsymbol{x}}$. If the residual corresponds to the coefficient vector $\vec{\boldsymbol{\rho}} = (\rho_e)_e$ with respect to the canonical dual basis of $\boldsymbol{\mathcal{ND}}_{1,\Gamma_D}(\mathcal{T}_l)$, we get

$$\left(\boldsymbol{\sigma}_l - A_l\widetilde{\boldsymbol{\xi}}_l, \mathbf{grad}\,\psi_{\boldsymbol{x}}\right)_{0;\Omega} = \sum_{e\in\mathcal{E}_l} \omega_e \cdot \rho_e \ . \tag{42}$$

The weights ω_e agree with the coefficients occurring in the representation of $\mathbf{grad}\,\psi_{\boldsymbol{x}}$ in the basis of the edge element space. Due to the small supports of $\psi_{\boldsymbol{x}}$ only a few ω_e are different from zero, namely those belonging to edges adjacent to $\boldsymbol{x}$. Moreover, the non–vanishing weights are either $+1$ or -1, depending on the orientation of the edge e. Thus, (42) can be implemented by summing up the weighted nodal values of all edges sharing the vertex $\boldsymbol{x}$.

For the sake of efficiency, it makes sense to rearrange the steps in which the computation of the correction in potential space is carried out; the residual can be calculated first, then it should be transferred to the dual space of $\mathcal{S}_{1,\Gamma_D}(\mathcal{T}_l)$ all at once: this amounts to the collective execution of the summing–up operation outlined above and can be characterised as the transpose of the transfer operator $T_l : \mathcal{S}_{1,\Gamma_D}(\mathcal{T}_l) \mapsto \boldsymbol{\mathcal{ND}}_{1,\Gamma_D}(\mathcal{T}_l)$ induced by the embedding $\mathbf{grad}\,\mathcal{S}_{1,\Gamma_D}(\mathcal{T}_l) \subset \boldsymbol{\mathcal{ND}}_{1,\Gamma_D}(\mathcal{T}_l)$.

If $\beta = 0$ in parts of the domain Ω, some local corrections in potential space may not be well defined. If we assume that σ is piecewise constant and bounded away from zero in $\mathrm{supp}(\sigma)$, which it usually is in real–life applications, then there is a ready remedy: The relaxation in $\mathcal{S}_{1,\Gamma_D}(\mathcal{T}_l)$ has to be confined to $\psi_{\boldsymbol{x}}$ such that $\mathrm{supp}(\psi_{\boldsymbol{x}}) \cap \mathrm{supp}(\sigma) \neq \emptyset$. This is natural, since outside $\mathrm{supp}(\sigma)$) the solution $\boldsymbol{E}$ of (17) is only unique up to an irrotational vectorfield. We point out that given the restricted correction in potential space, the multigrid algorithm can well cope with the semidefinite case.

The bottom line is that all steps of the algorithm involve purely local operations. This ensures computational costs for a single multigrid sweep.

7.4 Multigrid in the indefinite case

If $\beta < 0$, ellipticity may not only be infringed by the presence of a large kernel of the **curl**–operator, but also by negative eigenfunctions in its orthogonal complement. Nevertheless we aim to stick to the multigrid scheme designed in the previous sections.

Instead from the standard Helmholtz–decomposition now the analysis of the multigrid method should start from the $a(\cdot,\cdot)$–orthogonal splitting

$$\boldsymbol{\mathcal{ND}}_{1,\Gamma_D}(\mathcal{T}_L) = \boldsymbol{\mathcal{ND}}^0_{1,\Gamma_D}(\mathcal{T}_L) \oplus \mathcal{M}^- \oplus \mathcal{M}^+ \,,$$

where $\mathcal{M}^-$ and $\mathcal{M}^+$ are the spaces spanned by eigenfunctions of A_h belonging to negative and positive eigenvalues, respectively. It is easy to see that corrections in potential space are not affected in the indefinite case, as (26) remains valid. Conversely, we have to worry about the viability of the splitting (41).

Experience and theory (cf. [31]) teach us that a multigrid scheme for indefinite symmetric problems may perform well, if all vectorfields in $\mathcal{M}^-$ can be well represented on the coarsest grid. For moderate ratios β/α an elementary Fourier analysis shows that $\mathcal{M}^-$ only contains functions of long spatial wavelength.

To elaborate this further, we now focus on the time harmonic case, discussed in subsection 2.3, i.e., $\alpha = \mu^{-1}$ and $\beta = -\epsilon\omega^2$. For the moment assuming homogeneous material (i.e., $\mu, \epsilon = \text{const.}$), we conclude that a plane spatial wave $\boldsymbol{E}(\boldsymbol{x}) = \exp(i\boldsymbol{k}\boldsymbol{x}) \cdot \vec{\boldsymbol{e}}_x$ can only coincide with a negative eigenmode, if $|\boldsymbol{k}|^2 < \omega^2\mu\epsilon$. In other words, its spatial wavelength must be below a *critical wavelength* $\lambda_C := 2\pi/\omega\sqrt{\epsilon\mu}$.

According to Nyquist's theorem, we need at least two sampling points per wavelength to sample a sine wave. This heuristic gives us the following condition for an adequate representation of negative eigenmodes on $\mathcal{T}_0$: The length h_e of an edge e of the coarsest mesh $\mathcal{T}_0$ must satisfy

$$h_e \;\leq\; \frac{\lambda_C}{2} = \frac{\pi}{\omega\sqrt{\epsilon\mu}} \,, \tag{43}$$

where the maximal values of ϵ and μ in elements adjacent to e should be taken.

Note that on finer meshes the diameter of supports of nodal basis functions is well below the threshold (43). Thus even a plain Gauß–Seidel smoother is impervious to the impact of negative eigenmodes, since for any $\boldsymbol{\xi}_e$ we have $a(\boldsymbol{\xi}_e, \boldsymbol{\xi}_e) > 0$. This is, because the dominant frequency components of $\boldsymbol{\xi}_e$ belong to the space $\mathcal{M}^+$ spanned by eigenvectors corresponding to positive eigenvalues.

In sum, the multigrid convergence should not be affected by the presence of negative eigenvalues, if the above requirement (43) is met. In many applications computations are done at moderately high frequencies. Then, the performance of the multigrid method can be salvaged through sufficiently fine coarse grids without prohibitive costs.

As another precaution we can embed the V–cycle into a preconditioned conjugate residual method (PCR) [52]. This CG–variant is suitable for linear systems of equations with symmetric indefinite matrices. If the space $\mathcal{M}^-$ is poorly handled by the multigrid method, the CR–part may still effectively curb the error in $\mathcal{M}^-$.

8 Numerical results

At best, the rigorous theoretical results about the properties of the multigrid method and the error estimators provide norm equivalences with a guaranteed independence of the constants of certain parameters. However, there is hardly any information about the actual size of the constants. Moreover, rigorous theory fails in many cases relevant for practical applications, though the algorithms might still work well.

To offset these shortcomings of theoretical analysis it is badly recommended to study the behavior of the schemes in actual computations. This can at least confirm their viability for a few problems.

8.1 Multigrid convergence

We first study the convergence of multigrid V–cycles applied to (17) discretized by lowest order type–I edge elements for several model problems. To begin with, we focus on the case of regularly refined uniform hexahedral meshes. One Gauß–Seidel sweep is used for pre- and postsmoothing. We set the right hand side $\boldsymbol{f} = 0$ and provide a random initial guess. The rate of convergence is determined from the reduction of the Euclidean norm of the error in the final of 15 multigrid iteration sweeps. To offset the impact of randomness the average rate for two runs is calculated in each case.

The *first experiment* is carried out on a cube $\Omega :=]0;1[^3$ and we impose homogeneous Dirichlet boundary conditions on all of $\partial\Omega$. The coarsest grid $\mathcal{T}_0$ comprises eight equal cubes, which are successively regularly refined to create $\mathcal{T}_1, \ldots, \mathcal{T}_L$. We investigate the case of constant coefficients $\alpha \equiv 1$, $\beta = \text{const}$. The rates of convergence are measured for different depths L of refinement and various ratios α/β to study the influence of the relative scaling of the different parts of the bilinear form. The results are recorded in Tab. 1 for the V(1,1)–multigrid cycle (and for the preconditioned CG method, too). In addition, we monitor convergence in the absence of smoothing in potential space to underscore that multigrid efficiency critically hinges on it.

We observe the uniform boundedness of the convergence rates as predicted by the theory and, in addition, the robustness of the method with respect to α/β. This is particularly good news, since the method is to be employed in conjunction with implicit timestepping. In this case vulnerability to dominant zero order terms would impair the efficiency for small timesteps.

L	2	3	4	5	6
$\beta = 0.1$	**0.15** (5)[0.98]	**0.16** (5)[0.98]	**0.16** (5)[0.99]	**0.16** (5)[0.99]	**0.16** (5)[0.99]
$\beta = 0.5$	**0.15** (5)[0.97]	**0.16** (5)[0.97]	**0.16** (5)[0.98]	**0.16** (5)[0.98]	**0.16** (5)[0.99]
$\beta = 1.0$	**0.15** (5)[0.96]	**0.16** (5)[0.97]	**0.16** (5)[0.97]	**0.16** (5)[0.97]	**0.16** (5)[0.98]
$\beta = 2.0$	**0.15** (5)[0.96]	**0.16** (5)[0.96]	**0.16** (5)[0.96]	**0.16** (5)[0.97]	**0.16** (5)[0.98]
$\beta = 10.0$	**0.14** (5)[0.88]	**0.16** (5)[0.93]	**0.16** (5)[0.96]	**0.16** (5)[0.97]	**0.16** (5)[0.97]
$\beta = 100.0$	**0.10** (4)[0.75]	**0.13** (5)[0.91]	**0.15** (5)[0.92]	**0.16** (5)[0.95]	**0.16** (5)[0.96]

Table 1: *Convergence rates for multigrid V(1,1)–cycle obtained in numerical experiment 1. (In brackets: Average number of PCG steps needed to reduce the Euclidean norm of the residual by a factor of* 10^6*.)* [*In square brackets: Convergence rates without smoothing in potential space.*]

The *second experiment* relies on almost the same setting as the first, except for the domain, which is the three dimensional non–convex "L-shaped" domain $\Omega :=]0;1[^3/[0;\frac{1}{2}]^3$. The outcome of the second experiment is documented in Tab. 2. Despite the presence of a reentrant corner, we observe qualitatively the same behavior as in Exp. 1. This hints that irregularly shaped domains do not affect the method much.

We point out that the slight degradation of the multigrid convergence can be entirely avoided if a PCG–method is used (see Tab. 2)

L	2	3	4	5	6
$r = 0.1$	0.18 (5)	0.19 (5)	0.20 (5)	0.21 (5)	0.22 (5)
$r = 0.5$	0.18 (5)	0.19 (5)	0.20 (5)	0.21 (5)	0.22 (5)
$r = 1.0$	0.18 (5)	0.19 (5)	0.21 (5)	0.21 (5)	0.22 (5)
$r = 2.0$	0.17 (5)	0.19 (5)	0.21 (5)	0.21 (5)	0.22 (5)
$r = 10.0$	0.16 (4)	0.19 (5)	0.20 (5)	0.22 (5)	0.22 (5)

Table 2: *Multigrid convergence rates for Exp. 2. (In brackets: Required average number of PCG steps to reduce the norm of the residual by a factor of* 10^6*.)*

The *third experiment* is intended to probe the impact of strongly varying coefficient functions. It relies on the setting of the first numerical experiment and uses $\beta \equiv 1$. The coefficient α for the second order term was chosen according to

$$\alpha(\boldsymbol{x}) := \begin{cases} \alpha_0 & ; \text{ for } \boldsymbol{x} \in]1/3, 2/3[^3 \\ 1 & ; \text{ elsewhere in }]0, 1[^3 \end{cases} \tag{44}$$

The results are given in Tab. 3 and they highlight the amazing robustness of the method with respect to large jumps in the coefficient function $\alpha(\boldsymbol{x})$.

α_0	10^5	10^4	10^3	10^2	10^1	10^{-1}	10^{-2}	10^{-3}	10^{-4}	10^{-5}
$L = 2$	0.15	0.17	0.16	0.16	0.16	0.18	0.20	0.20	0.20	0.24
$L = 3$	0.23	0.18	0.18	0.17	0.17	0.18	0.20	0.22	0.21	0.25
$L = 4$	0.24	0.21	0.21	0.20	0.19	0.19	0.22	0.23	0.22	0.26
$L = 5$	0.23	0.22	0.19	0.18	0.17	0.17	0.22	0.23	0.23	0.26

Table 3: *Convergence rates for multigrid V(1,1)–cycle in the case of jumping coefficient* α *(Exp. 3).*

In the *forth experiment* the jump in the coefficient occurs in the zero order term, by choosing β according to (44) and $\alpha \equiv 1$. Everything else remains unchanged compared to the previous experiment. Tab. 4 illustrates the behavior of the rate of convergence. It reveals satisfactory convergence regardless of strong variations in $\beta(\boldsymbol{x})$.

β_0	10^5	10^4	10^3	10^2	10^1	10^{-1}	10^{-2}	10^{-3}	10^{-4}	10^{-5}
$L = 2$	0.32	0.22	0.19	0.22	0.20	0.16	0.16	0.16	0.16	0.16
$L = 3$	0.30	0.23	0.23	0.24	0.22	0.18	0.19	0.19	0.19	0.20
$L = 4$	0.25	0.24	0.24	0.26	0.23	0.20	0.21	0.21	0.21	0.21
$L = 5$	0.25	0.26	0.26	0.26	0.24	0.22	0.23	0.23	0.23	0.23

Table 4: *Convergence rates for multigrid V(1,1)–cycle in the case of jumping coefficient* β *(Exp. 4).*

The *fifth experiment* was dealing with an even more challenging case of jumping coefficients, described by $\beta \equiv 1$ and

$$\alpha(\boldsymbol{x}) := \begin{cases} \alpha_0 & \text{for } \boldsymbol{x} \in \boldsymbol{C}_1 \cup \boldsymbol{C}_2 \cup \boldsymbol{C}_3 \cup \boldsymbol{C}_4 \\ 1 & \text{elsewhere ,} \end{cases} \tag{45}$$

where

$$\boldsymbol{C}_1 :=]0, \frac{1}{2}[^3 \qquad \boldsymbol{C}_2 :=]\frac{1}{2}, 1[^2 \times]0, \frac{1}{2}[$$
$$\boldsymbol{C}_3 :=]\frac{1}{2}, 1[\times]0, \frac{1}{2}[^2 \qquad \boldsymbol{C}_4 :=]\frac{1}{2}, 1[\times]0, \frac{1}{2}[\times]\frac{1}{2}, 1[\, .$$

This particular arrangement of jumps is called non–monotonous. Recent results reveal that this type of jumps wreaks havoc to the convergence of standard multigrid for second order problems [42].

The resulting rates of convergence are recorded in Tab. 5, as well as the iteration counts for the preconditioned CG method. The message sent by the figures in Tab. 5 is daunting; little remains of the uniform rate of convergence in a practical range of refinement levels. In this sense, our method behaves exactly like conventional multigrid [42]. We also found that using the V–cycle in conjunction with a preconditioned CG method does not cure the overall deterioration of the rates of convergence on finer levels.

α_0	10^5	10^4	10^3	10^2	10^1	10^{-1}	10^{-2}	10^{-3}	10^{-4}	10^{-5}
$L = 2$	0.45	0.44	0.44	0.43	0.32	0.29	0.37	0.41	0.41	0.42
$L = 3$	0.54	0.54	0.53	0.51	0.35	0.32	0.48	0.48	0.50	0.51
$L = 4$	0.61	0.62	0.62	0.57	0.38	0.36	0.53	0.57	0.59	0.59
$L = 5$	0.69	0.68	0.68	0.65	0.41	0.381	0.59	0.65	0.66	0.67
$L = 6$	0.74	0.74	0.73	0.70	0.43	0.41	0.65	0.70	0.72	0.73

Table 5: *Convergence rates for multigrid V(1,1)–cycle in the case of a coefficient α governed by (45) (Exp. 5).*

The *sixth experiment* deals with the behavior of the multigrid V(1,1)–cycle on locally refined unstructured tetrahedral meshes. Throughout, we use it as preconditioner in the framework of a PCG method and measure the number of iterations needed to achieve a reduction of the norm of the residual by a factor of 10^{10}. We resort to an L-shaped domain $\Omega \in \mathbb{R}^3$ representing a cube from which the fourth quadrant of the x-y-plane had been cut out: $\Omega := [-1, 1]^3 \setminus \{[0, 1] \times [-1, 0] \times [-1, 1]\}$ (see Fig. 3)

We split the domain into two subregions $\Omega_1 := [-1, 0] \times [0, 1] \times [-1, 1]$ and $\Omega_2 := \Omega \setminus \Omega_1$. On Ω_1, which comprises the second quadrant of the x-y-plane, α and β are always set to 1, whereas on Ω_2 these coefficients (denoted by α_2 and β_2 in the tables below) vary by several orders of magnitude in order to obtain steep jumps.

Again, we solve problem (17), discretized by means of lowest order tetrahedral edge elements. The right hand side $\boldsymbol{f}$ is a constant vector field $f_x = -1,\ f_y = 1,\ f_z = 0$. Natural boundary conditions ($\boldsymbol{n} \times \mathbf{curl}\, \boldsymbol{E} = 0$) are applied on the planes $z = 1$ and $z = -1$ and homogeneous Dirichlet boundary conditions ($\boldsymbol{n} \times \boldsymbol{E} = 0$) on the remaining

surfaces. Thus we create a rather challenging problem: The solution has a singularity along the edge $\{x = 0, y = 0\}$ where the material coefficients of the three adjoining regions are varying by several orders of magnitude.

We started with a coarse grid $\mathcal{T}_0$ consisting of 52 tetrahedra as shown in Fig. 3. The mesh was refined adaptively by employing the hierarchical error estimator of Sect. 6.2. The results are given in Tab. 6. Compared to the structured grids, we observe that convergence is only about half as fast. This seems to be the fault of the tetrahedra, since a similar loss of speed is also encountered for Lagrangian finite elements and standard multigrid when switching to simplicial meshes. However, adaptive refinement itself does not have a harmful impact. The degradation noticeable in the bottom row of Tab. 6 is probably due to the non–monotonous jump of the coefficient α (cf. Exp. 5).

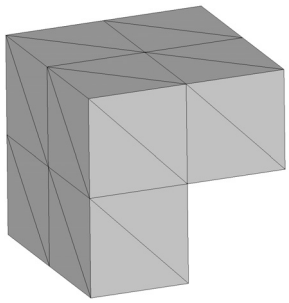

Figure 3: *Coarse grid for the L-shaped domain.*

	Level	1	2	3	4	5	6	7
α_2	β_2							
1	1	17	18	18	18	18	19	20
1	10^4	15	15	16	17	17	17	17
1	10^{-4}	18	17	18	19	20	21	23
10^4	1	16	18	21	17	18	19	21
10^{-4}	1	19	17	19	19	25	31	36

Table 6: Exp. 6: *Number of PCG-iterations required to reduce the initial residual by a factor* 10^{10}.

For the case $\alpha_2 = \beta_2 = 1$ Fig. 4 depicts a cross section (lying in the x-y-plane) of the locally refined grid and the solution. Both plots were generated on the fifth refinement level and show the improved mesh resolution along the edge $\{x = 0, y = 0\}$ where the vector field is singular.

For $\alpha_2 = 1, \beta_2 = 10^4$ similar plots are shown in Fig. 5. Now, the vector field is concentrated in the subdomain Ω_1 and the mesh has become finer near the internal boundary between Ω_1 and Ω_2.

8.2 Performance of error estimators

In the *seventh experiment* we tested the performance of the error estimators for the variational problem (17) on $\Omega := [0, 1]^3$ and Dirichlet boundary conditions throughout. The coefficients α and β from (17) were kept constant all over the domain; α is always set to 1. On the other hand, we took into account different values for β in order to obtain situations resembling an implicit time–stepping scheme with widely varying

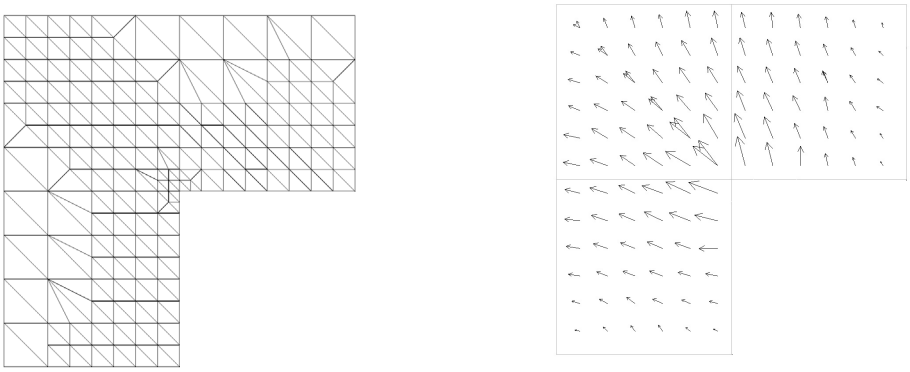

Figure 4: *Cross section of the locally refined grid and the vector field for the case* $\alpha_2 = \beta_2 = 1$ *(Exp. 6).*

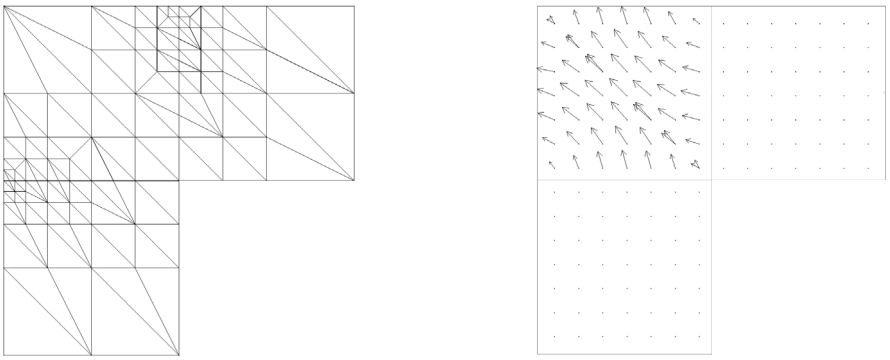

Figure 5: *Cross section of the locally refined grid and the vector field for the case* $\alpha_2 = 1$, $\beta_2 = 10^4$ *(Exp. 6).*

time steps. We remark that boundary data and the right hand side were chosen to produce the smooth solution $\boldsymbol{E} = (0, 0, \sin(\pi x)$.

We define an effectivity index $\varepsilon := \eta_{Est}/\eta_{True}$ as the ratio between the estimated and the true discretization error. The results for the hierarchical estimator, which was introduced in Sect. 6.2, are given in Tab. 7. Evidently the desired asymptotic limit

Level	0	1	2	3	4	5
$\beta = 10^{-4}$	0.45	0.63	0.67	0.69	0.69	0.70
$\beta = 10^{-2}$	0.45	0.63	0.67	0.69	0.69	0.70
$\beta = 1$	0.46	0.67	0.72	0.75	0.76	0.77
$\beta = 10^{2}$	0.65	1.01	1.01	1.04	1.06	1.07
$\beta = 10^{4}$	0.74	1.27	1.40	1.43	1.33	1.19

Table 7: *Effectivity index ε for the hierarchical error estimator on the unit cube (Exp. 7).*

$\varepsilon \to 1$ is not approached for $\beta \leq 1$. On the other hand, the error is over–estimated in the remaining cases. As noted in Sect. 6.2, the estimator solves the defect equation for the hierarchical surplus by one step of a block-Jacobi iteration. For low β this procedure effectively acts a smoother, whereas for high β the mass–term $(\beta \boldsymbol{E}, \boldsymbol{\eta})_{0;\Omega}$ is dominating in (17).

In the latter case the solution of the defect equation resembles an L_2–projection, for which the decoupling of basis functions in the hierarchical surplus not appropriate. In general, a possible remedy may be the stabilization of the mass–matrix by lumping. But there is no simple lumping procedure available for Nédélec-spaces, so we tried to improve the estimator by forgoing decoupling in the hierarchical surplus. The results are shown in Tab. 8 and appear to be very satisfactory. However, this procedure was much more expensive and did not produce significantly different grids in the adaptive refinement steps. The effectivity indices for the residual based estimator are shown in Tab. 9.

Level	0	1	2	3	4	5
$\beta = 10^{-4}$	0.25	0.88	0.89	0.93	0.95	0.96
$\beta = 10^{-2}$	0.25	0.94	0.89	0.93	0.95	0.96
$\beta = 1.0$	0.26	0.92	0.90	0.94	0.95	0.96
$\beta = 10^{2}$	0.44	0.59	0.92	0.96	0.98	0.99
$\beta = 10^{4}$	0.54	0.35	0.95	0.97	0.98	0.98

Table 8: *Effectivity index ε for the hierarchical error estimator on the unit cube without decoupling in the hierarchical surplus. (Exp. 7)*

Please note that the residual based error estimator in general provides only estimates for a scaled norm of the error. What is important is the correct information about the distribution of the error. Crucial for this purpose is that the effectivity index reaches a stable limit on finer discretizations. This is confirmed by the values for ε from Tab. 9.

Level	0	1	2	3	4	5
$\beta = 10^{-4}$	4.05 (2.40)	8.05 (4.18)	8.18 (4.49)	8.24 (4.57)	8.27 (4.59)	8.29 (4.59)
$\beta = 10^{-2}$	4.04 (2.40)	8.05 (4.18)	8.17 (4.49)	8.23 (4.57)	8.27 (4.59)	8.29 (4.59)
$\beta = 1.0$	3.01 (2.37)	7.64 (4.20)	7.78 (4.53)	7.84 (4.62)	7.87 (4.65)	7.89 (4.66)
$\beta = 10^{2}$	2.29 (2.28)	4.27 (4.25)	4.70 (4.67)	4.95 (4.88)	5.20 (4.97)	5.26 (5.01)
$\beta = 10^{4}$	2.33 (2.31)	4.23 (4.22)	4.66 (4.65)	4.86 (4.86)	4.95 (4.94)	5.00 (4.99)

Table 9: *Effectivity ε for the residual based error estimator on the unit cube (Exp. 7). The number in brackets show ε, if the contribution of the inner residual is neglected*

When we quantitatively compare the various terms which are summed up in this estimator, then the first part of the **curl**-related contribution $\eta_T^{\perp}$ in (34), i.e. the inner residual, appears to be critical. This may be due to the fact that we are dealing with the lowest order Nédélec-space where $\mathbf{curl}\,\alpha\,\mathbf{curl}\,\boldsymbol{E}_h$ vanishes and thus a certain contribution of the residual is dropped. So we repeat our calculations, this time omitting the inner residual completely. Then the results are more satisfactory (see Tab. 9.

Although appearing less reliable, this estimator is more economic concerning computation time and memory usage. In our implementation it was approximately three times faster than its hierarchical counterpart.

In the *eighth experiment* we revert to the setting of Exp. 6. As there is no analytical solution available, we take the field computed on refinement level 7 as a substitute for the exact solution. The results are shown in the Tabs. 10 and 11. Also in the presence of field singularities and steep material jumps the estimates remain within a reliable range.

	Level	0	1	2	3	4	5
α_2	β_2						
1	1	0.84	0.87	0.84	0.89	0.89	0.97
1	10^{4}	0.74	0.70	0.58	0.62	0.69	0.82
1	10^{-4}	0.57	0.53	0.52	0.53	0.54	0.58
10^{4}	1	0.77	0.81	0.82	0.86	0.87	0.99
10^{-4}	1	0.80	0.88	0.95	0.96	1.04	1.07

Table 10: *Exp. 8: Estimated effectivity ε for the hierarchical error estimator on the L-shaped domain with varying coefficients α_2 and β_2.*

Without recording the related values we point out that the procedures mentioned in the previous section – a modified solver for the hierarchical surplus and the neglect of the inner residual – yielded improved results.

8.3 The time–harmonic case: waveguide computations

Here we consider the scattering of an electric field by a so–called taper structure, a device which is used to connect waveguides of different shape. In our example two rectangular microstrip–lines of different width form the input and output ports of

	Level	0	1	2	3	4	5
α_2	β_2						
1	1	5.84	6.88	6.61	6.91	6.74	6.83
1	10^4	7.56	9.41	8.24	7.74	7.18	6.60
1	10^{-4}	5.11	3.93	3.61	3.26	3.52	3.60
10^4	1	7.33	9.23	9.06	8.86	9.28	10.5
10^{-4}	1	3.19	3.44	3.36	3.55	3.94	4.46

Table 11: *Exp. 8: Estimated effectivity ε for the residual based error estimator on the L-shaped domain with varying coefficients α_2 and β_2.*

the device, the taper section is placed in the middle of the model (see Fig. 6). We enclose the whole arrangement by a metallic box. All conductors are supposed to have negligible resistance, so that the tangential components of the electric field vanish on their surfaces (this is a sensible assumption if the skin depth is small).

The stripline is placed on a dielectric substrate with $\epsilon = 100$ and $\mu = 1$; the remaining region is air ($\epsilon = \mu = 1$). The taper device is fed on the input port by a quasi–TEM–wave, which is partially reflected at the taper section.

We assume that at both ports (formed by the front and back plane) only quasi–TEM–modes are propagated. Thus, in the immediate vicinity of each port the field may be split into an incident and a reflected TEM–wave by [84]

$$\widehat{\boldsymbol{E}}(\boldsymbol{x}) = \widehat{\boldsymbol{E}}_{inc}(\boldsymbol{x}) \;+\; \widehat{\boldsymbol{E}}_{ref}(\boldsymbol{x}) = \widehat{\boldsymbol{E}}_{inc}(x,y)\, e^{-i\zeta z} \;+\; \widehat{\boldsymbol{E}}_{ref}(x,y)\, e^{i\zeta z}\ .$$

The direction of propagation is aligned with the z-axis; ζ denotes the propagation constant and is given by $\zeta = \omega\sqrt{\epsilon\mu}$. By applying the operator $\boldsymbol{n} \times \mathbf{curl}$ to (8.3), we obtain a Cauchy-type boundary condition similar to (11) on the ports. The incident field $\widehat{\boldsymbol{E}}_{inc}(x,y)$ of a TEM–mode can be derived from a two–dimensional static potential for which Laplace's equation holds on the plane defining the port [84].

Thus we finally arrive at the variational formulation (16) in Sect. 2.3. We have to tackle an indefinite problem with complex fields, which have singular behavior along the edges of the striplines.

All computations were started on the initial mesh shown in Fig. 6, which comprises 566 degrees of freedom. The figure also displays the grid and the electric field after two steps of adaptive refinement. We applied two different excitation frequencies $\omega = 0.02\,\pi$ and $\omega = 2\,\pi$ to assess the influence of the ratio r between grid spacing and local wavelength λ_C

$$r = \max \frac{h_T}{\lambda_C}\ , \qquad \lambda_C = \frac{2\pi}{\omega\sqrt{\epsilon\mu}}$$

For $\omega = 2\,\pi$ we have $r = 0.49$ and thus are reaching the critical coarse grid limit $r = 0.5$ on our initial mesh $\mathcal{T}_0$ (see Sect. 7.4).

Tab. 12 records the behavior of the PCR–method preconditioned with a multigrid V(1,1)–cycle. As was to be expected, the convergence rates are better for the low frequency, where the coarse mesh provides a superior resolution of $\mathcal{M}^-$. But even for the high frequency range no substantial deterioration of the solver could be observed.

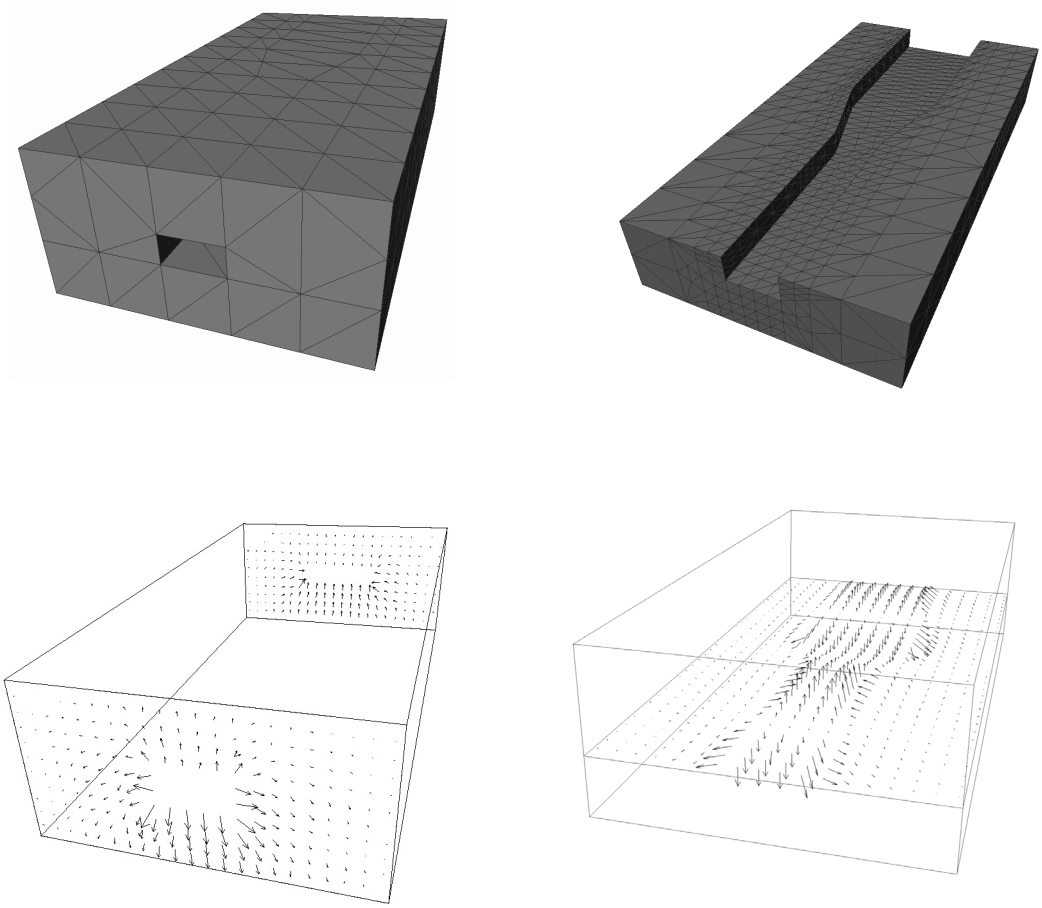

Figure 6: *Cross section of the locally refined grid and the vector field for* $\omega = 2\,\pi$.

For the sake of comparison we solved the problem again, now omitting the smoothing in the potential space. The results in Tab. 12 demonstrate the disastrous consequences. As the figures reveal, the convergence rates are worse for the low frequency. This is due to the fact that here we are rather close to the static limit, where the solution behaves like a potential field (Observe that the incident TEM–wave is derived from a static solution).

Level	r	1	2	3	4	5	6	7
$\omega = 0.02\,\pi$	0.0049	22 (604)	21 (5934)	21 (16983)	21 (37363)	21	22	23
$\omega = 2\,\pi$	0.49	31 (239)	31 (1414)	29 (3539)	28 (6729)	30	31	34

Table 12: *Waveguide problem: Number of PCR-iterations required to reduce the initial residual by a factor* 10^{10}*. Iteration counts in brackets result if smoothing in potential space is omitted.*

Next we examine the capability of the error estimators introduced before, to serve as error indicators in the indefinite case. Although our problem is *formally* an elliptic one, it is nevertheless derived from a system of *hyperbolic* equations and thus exhibits their typical propagation effects due to solution components in $\mathcal{M}^-$. Thus we may encounter oscillatory solutions where sources (and thus also unwanted effects generated by discretization errors) may produce far–reaching field contributions which cannot be captured by local error estimators.

However, it may be still sensible to detect and refine areas contributing large errors in the high-frequency components of the solution. Such regions typically appear near field singularities or near interfaces between materials with varying coefficients.

Here we measure the error $\widehat{\boldsymbol{\xi}}$ in the norm

$$\left(\frac{1}{\mu}\,\mathbf{curl}\,\widehat{\boldsymbol{\xi}}, \mathbf{curl}\,\widehat{\boldsymbol{\xi}}\right)_{0;\Omega} + \left(\omega^2\epsilon\widehat{\boldsymbol{\xi}}, \widehat{\boldsymbol{\xi}}\right)_{0;\Omega} + \left(\frac{\omega}{\mu c}\widehat{\boldsymbol{\xi}} \times \boldsymbol{n}, \widehat{\boldsymbol{\xi}} \times \boldsymbol{n}\right)_{0;\Omega} \tag{46}$$

which is derived from (16) by switching from negative to positive signs. To get an idea of the quality of the proposed error indicators, we compare our solutions to the one obtained on the seventh level, considering the latter as a good approximation of the exact solution.

The critical phase within of the hierarchical error estimator appears to be the block-Jacobi step for obtaining an approximate solution of the hierarchical defect system. As the system matrix contains negative eigenvalues, the Jacobi step amplifies the related eigenmodes. However, if the grids are not too coarse, the modulus of all negative eigenvalues is comparatively small and these modes can be expected to give only minor contributions.

The residual based estimator is applied without any alterations, as its different contributions are simply added up anyway. Table 13 gives the results, which exhibit a behavior similar to those of the positive definite case.

In order to demonstrate the gains through error estimation and local grid refinement, we have monitored the decrease of the discretization error η_{True} for $\omega = 2\pi$ in Fig. 7. The adaptively constructed grids bring about a major saving in the number of unknowns.

Level	0	1	2	3	4	5	error indicator
$\omega = 0.02\,\pi$	0.79	0.78	0.80	0.85	0.89	1.02	*hierarchical*
$\omega = 2\,\pi$	0.67	0.69	0.78	0.81	0.88	0.97	
$\omega = 0.02\,\pi$	3.84	4.00	4.27	4.46	4.72	5.42	*residual based*
$\omega = 2\,\pi$	3.41	4.41	4.77	4.94	5.47	5.81	

Table 13: *Waveguide problem: estimated effectivity index ε of the error estimators.*

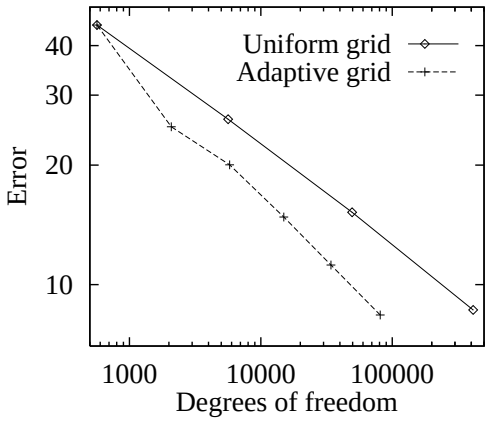

Figure 7: *Decrease of the discretization error η_{True} on uniformly and adaptively refined grids.*

References

[1] B. Achchab, A.Agouzal, J. Baranger, and J. Maitre, *Estimateur d'erreur a posteriori hiérarchique. Application aux éléments finis mixtes*, Tech. Rep. 212, Equipe d'Analyse Numérique, Lyon Saint-Etienne, C.N.R.S. U.R.A. 740, 1995.

[2] A. Alonso, *Error estimators for a mixed method*, Numer. Math., 74 (1996), pp. 385–395.

[3] C. Amrouche, C. Bernardi, M. Dauge, and V. Girault, *Vector potential in three–dimensional nonsmooth domains*, Tech. Rep. 96–04, IRMAR, Rennes, France, 1996.

[4] I. Babuška and W. Rheinboldt, *Error estimates for adaptive finite element computations*, SIAM J. Numer. Anal., 15 (1978), pp. 736–754.

[5] E. Baensch, *Local mesh refinement in 2 and 3 dimensions*, IMPACT Comput. Sci. Engrg., 3 (1991), pp. 181–191.

[6] D. Baldomir, *Differential forms and electromagnetism in 3–dimensional Euclidean space $\mathbb{R}^3$.*, IEE Proc. A, 133 (1986), pp. 139–143.

[7] R. Bank, A. Sherman, and A. Weiser, *Refinement algorithm and data structures for regular local mesh refinement*, in Scientific Computing, R. Stepleman et al., ed., vol. 44, IMACS North–Holland, Amsterdam, 1983, pp. 3–17.

[8] R. Bank and A. Weiser, *Some a posteriori error estimators for elliptic partial differential equations*, Math. Comp., 44 (1985), pp. 283–301.

[9] R. Bank and B. Welfert, *A posteriori error estimates for the Stokes equations: A comparison elliptic partial differential equations*, Comp. Meth. Appl. Mech. Engrg., 87 (1990), pp. 323–340.

[10] R. Beck and R. Hiptmair, *Multilevel solution of the time-harmonic Maxwell equations based on edge elements*, Tech. Rep. SC-96-51, ZIB Berlin, 1996, submitted to Int. J. Num. Meth. Eng.

[11] R. Beck, R. Hiptmair, R. Hoppe, and B. Wohlmuth, *Residual based a posteriori error estimators for curl–conforming finite element approximations*, tech. rep., Institut für Mathematik, Universität Augsburg, 1997. in preparation.

[12] ——, *A hierarchical error for H(curl)–elliptic problems*, tech. rep., Institut für Mathematik, Universität Augsburg, 1998. in preparation.

[13] R. Becker and R. Rannacher, *A feed-back approach to error control in finite element methods: Basic analysis and examples*, East-West J. Numer. Math., 4 (1996), pp. 237–264.

[14] ——, *Weighted a posteriori error control in FE methods*, Tech. Rep. 96 - 1, SFB 359 - Universität Heidelberg, Januar 1996.

[15] J. Berenger, *A perfectly matched layer for the absorption of electromagnetic waves*, J. Comp. Phys., 114, pp. 185-200 (1994).

[16] J. Bey, *Tetrahedral grid refinement*, Computing, 55 (1995), pp. 355–378.

[17] C. Biddlecomb, E. Heighway, J. Simkin, and C. Trowbridge, *Methods for eddy current computation in three dimensions*, IEEE Trans. Mag., 18 (1982), pp. 492–497.

[18] O. Biro and K. Preis, *On the use of the magnetic vector potential in the finite element analysis of three-dimensional eddy currents*, IEEE Trans. Magn., 25 (1989), pp. 3145–3159.

[19] O. Biro, K. Preis, K. Richter, and G. Vrisk, *Performance of different vector potential formulations in solving multiply connected 3D eddy current problems*, IEEE Trans. Mag., 26 (1990), pp. 438–441.

[20] D. Boffi, P. Fernandes, L. Gastaldi, and I. Perugia, *Compuational models of electromagnetic resonators: Analysis of edge element approximation*, SIAM J. Numer. Anal., (1997). submitted.

[21] A. Bonnet-BenDhia, C. Hazard, and S. Lohrengel, *A singular field method for the solution of Maxwell's equations in polyhedral domains*, Tech. Rep. 299, ENSTA, 1997.

[22] F. Bornemann, B. Erdmann, and R. Kornhuber, *A posteriori error estimates for elliptic problems in two and three spaces dimensions*, SIAM J. Numer. Anal, 33 (1996), pp. 1188–1204.

[23] A. Bossavit, *Mixed finite elements and the complex of Whitney forms*, in The Mathematics of Finite Elements and Applications VI, J. Whiteman, ed., Academic Press, London, 1988, pp. 137–144.

[24] ——, *Whitney forms: A class of finite elements for three–dimensional computations in electromagnetism*, IEE Proc. A, 135 (1988), pp. 493–500.

[25] ——, *Solving Maxwell's equations in a closed cavity and the question of spurious modes*, IEEE Trans. Mag., 26 (1990), pp. 702–705.

[26] ——, *Mixed methods and the marriage between mixed finite elements and boundary elements*, Num. Meth. Part. Diff. Equ., 7 (1991), pp. 347–362.

[27] ——, *A new viewpoint on mixed elements*, Meccanica, 27 (1992), pp. 3–11.

[28] ——, *Électromagnétisme, en vue de la modélisation*, Springer–Verlag, Paris, 1993.

[29] D. Braess and R. Verfürth, *A posteriori error estimators for the Raviart-Thomas element*, SIAM F. Numer. Anal., 33 (1996), pp. 2431–2445.

[30] J. Bramble, *Multigrid methods*, Pitman Research Notes in Mathematics Series, Longman, London, 1993.

[31] J. Bramble, D. Kwak, and J. Pasciak, *Uniform convergence of multigrid v-cycle iterations for indefinite and nonsymmetric problems*, SIAM J. Numer. Anal., 31 (1994), pp. 1746–1763.

[32] A. Brandt, *Multigrid Techniques: 1984 Guide with Applications*, vol. 5 of GMD–Studien, GMD, Bonn, 1984.

[33] S. Brenner and R. Scott, *Mathematical theory of finite element methods*, Texts in Applied Mathematics, Springer–Verlag, New York, 1994.

[34] C. Carstensen and S. Jansche, *A posteriori error estimates and adaptive mesh-refining for non-conforming finite element methods*. to appear in Numer. Math.

[35] Z. Chen, M. Ney, and W. Hoefer, *A new finite-difference time-domain algorithm formulation and its equivalence with the TLM symmetrical condensed node*, IEEE Trans. Microw. Theory Tech., 39 (1991), pp. 2160–2168.

[36] P. Ciarlet, *The finite element method for elliptic problems*, North-Holland, Amsterdam, 1978.

[37] P. Clément, *Approximation by finite element functions using local regularization*, RAIRO Anal. Numér., 2 (1975), pp. 77–84.

[38] F. Cooray and G. Costache, *An overview of the absorbing boundary conditions*, J. Electromagn. Waves Appl., 5 (1991).

[39] M. Costabel and M. Dauge, *Singularities of electromagnetic fields in polyhedral domains*, tech. rep., IRMAR, Rennes, 1997.

[40] P. Deuflhard, P. Leinen, and H. Yserentant, *Concepts of an adaptive hierarchical finite element code*, IMPACT Comput. Sci. Engrg., 1 (1989), pp. 3–35.

[41] B. Dillon and J. Webb, *A comparison of formulations for the vector finite element analysis of waveguides*, IEEE Trans. Microw. Theory Tech., 42 (1994), pp. 308–316.

[42] M. Dryja, M. Sarkis, and O. Widlund, *Multilevel Schwarz methods for elliptic problems with discontinuous coefficients in three dimensions*, Numer. Math., 72 (1996), pp. 313–348.

[43] R. Duran and R. Rodriguez, *On the asymptotic exactness of Bank-Weiser's estimator*, Numer. Math., 62 (1992), pp. 297–303.

[44] B. Engquist and A. Majda, *Absorbing boundary conditions for the numerical solution of waves*, Math. Comp., 31, pp. 629-651 (1977).

[45] K. Erikson, D. Estep, P. Hansbo, and C. Johnson, *Introduction to adaptive methods for differential equations*, Acta Numerica, (1995), pp. 105–158.

[46] K. Eriksson and C. Johnson, *An adaptive finite element method for linear elliptic problems*, Math. Comput., 50 (1988), pp. 361–383.

[47] ——, *Adaptive finite element methods for parabolic problems. iv: Nonlinear problems*, SIAM J. Numer. Anal., 32 (1995), pp. 1729–1749.

[48] P. Fernandes and G. Gilardi, *Magnetostatic and electrostatic problems in inhomogeneous anisotropic media with irregular boundary and mixed boundary conditions*, M^3AS, 7 (1997), pp. –. to appear.

[49] V. Girault and P. Raviart, *Finite element methods for Navier–Stokes equations*, Springer–Verlag, Berlin, 1986.

[50] D. Givoli, *Numerical Methods for Problems in Infinire Domains*, Elsevier, Amsterdam, 1992.

[51] W. Hackbusch, *Theorie und Numerik elliptischer Differentialgleichungen*, B.G. Teubner–Verlag, Stuttgart, 1986.

[52] ——, *Iterative Lösung großer linearer Gleichungssysteme*, B.G. Teubner–Verlag, Stuttgart, 1991.

[53] R. Hiptmair, *Canonical construction of finite elements*, Tech. Rep. 360, Institut für Mathematik, Universität Augsburg, 1996. to appear in Math. Comp.

[54] ——, *Multigrid method for Maxwell's equations*, Tech. Rep. 374, Institut für Mathematik, Universität Augsburg, 1997. Submitted to SINUM.

[55] R. Hiptmair and A. Toselli, *Overlapping Schwarz methods for vector valued elliptic problems in three dimensions*, Tech. Rep. 747, Courant Institute,New York, 1997.

[56] R. Hoppe and B. Wohlmuth, *Adaptive multilevel iterative techniques for nonconforming finite element discretizations*, East-West J. Numer. Math., 3 (1995), pp. 179–197.

[57] ——, *A comparison of a posteriori error estimators for mixed finite elements*, Tech. Rep. 350, Math.–Nat. Fakultät, Universität Augsburg, 1996. to appear in Math. Comp.

[58] ——, *Element-oriented and edge-oriented local error estimators for nonconforming finite element methods*, M^2AN Math. Modelling and Numer. Anal., 30 (1996), pp. 237–263.

[59] ——, *Adaptive multilevel techniques for mixed finite element discretizations of elliptic boundary value problems*, SIAM J. Numer. Anal., 34 (1997), pp. 1658–1687.

[60] ——, *Multilevel iterative solution and adaptive mesh refinement for mixed finite element discretizations*, Appl. Num. Math, 23 (1997), pp. 97–117.

[61] J. Jin, *The Finite Element Method in Electrodynamics*, Wiley, New York, 1993.

[62] C. Johnson and P. Hansbo, *Adaptive finite element methods in computational mechanics*, Comp. Meth. Appl. Mech. Eng., 101 (1992), pp. 143–181.

[63] A. Kost, *Numerische Methoden in der Berechnung elektromagnetischer Felder*, Springer, Berlin, 1994.

[64] J.-F. Lee, R. Lee, and A. Cangellaris, *Time-domain finite element methods*, IEEE Ant. Prop., 45 (1997), pp. 430–441.

[65] P. Leonard and D. Rodger, *Finite element scheme for transient 3D eddy currents*, IEEE Trans. Magn., 24 (1988), pp. 90–93.

[66] K. Mahadevan, R. Mittra, and P. Vajda, *Use of Whitney edge and face element for efficient finite element time domain solution of Maxwell's equations*, J. Electrom. Waves and Appl., 8 (1994), pp. 1173–1191.

[67] G. Makridakis and P. Monk, *Time–discrete finite element schemes for Maxwell's equations*, RAIRO M^2AN, 29 (1995), pp. 171–197.

[68] W. Mitchell, *Unified multilevel adaptive finite element methods for elliptic problems*, Tech. Rep. UIUCDCS–R–88–1436, University of Illinois, 1988.

[69] P. Monk, *An analysis of a mixed method for approximating Maxwell's equations*, SIAM J. Numer. Anal., 28 (1991), pp. 1610–1634.

[70] ——, *Analysis of a finite element method for Maxwell's equations*, SIAM J. Numer. Anal., 29 (1992), pp. 714–729.

[71] ——, *A finite element method for approximating the time–harmonic Maxwell equations*, Numer. Math., 63 (1992), pp. 243–261.

[72] ——, *An analysis of Nédélec's method for the spatial discretization of Maxwell's equations*, J. Comp. Appl. Math., 47 (1993), pp. 101–121.

[73] ——, *On the p and hp–extension of Nédélec's conforming elements*, J. Comp. Appl. Math., 53 (1994), pp. 117–137.

[74] ——, *Superconvergence of finite element approximations to Maxwell's equations*, Num. Meth. Part. Diff. Equ., 10 (1994), pp. 793–812.

[75] P. Monk and A. Parrot, *A dispersion analysis of finite element methods for Maxwell's equations*, SIAM J. Sci. Comp., 15 (1994), pp. 916–937.

[76] P. Monk and E. Süli, *A convergence analysis of Yee's scheme on nonuniform grids*, SIAM J. Numer. Anal., 31 (1994), pp. 393–412.

[77] G. Mur, *Absorbing boundary conditions for the finite-difference approximation of the time domain electromagnetic field equation*, IEEE Trans. Electromagn. Compat., 23 (1981).

[78] J. Nédélec, *Mixed finite elements in* R^3, Numer. Math., 35 (1980), pp. 315–341.

[79] ——, *A new family of mixed finite elements in* R^3, Numer. Math., 50 (1986), pp. 57–81.

[80] P. Oswald, *Multilevel finite element approximation*, Teubner Skripten zur Numerik, B.G. Teubner, Stuttgart, 1994.

[81] J. P. Ciarlet and J. Zou, *Fully discrete finite element approaches for time–dependent Maxwell equations*, Tech. Rep. TR MATH–96-31 (105), Department of Mathematics, The Chinese University of Hong Kong, 1996.

[82] K. Paulsen, D. Lynch, and J. Strohbehn, *Three–dimensional finite, boundary and hybrid element solution of the Maxwell equations for lossy dielectric media*, IEEE Trans. Microwave Theory Tech., 36 (1993), pp. 682–693.

[83] K. D. Paulsen, D. R. Lynch, and J. W. Strobehn, *Three-dimensional finite, boundary and hybrid element solutions of the Maxwell equations for lossy dielectric media*, IEEE Trans. Microw. Theory Tech., 36 (1988).

[84] S. Ramo, J. R. Whinnery, and T. van Duzer, *Fields and Waves in Communication Electronics*, Wiley, New–York, 1984.

[85] L. R. Scott and Z. Zhang, *Finite element interpolation of nonsmooth functions satisfying boundary conditions*, Math. Comp., 54 (1990), pp. 483–493.

[86] J. Shen, *Computational Electromagnetics Using Boundary Elements*, Computational Mechanics Publications, Southampton, Boston, 1994.

[87] P. P. Silvester and R. L. Ferrari, *Finite Elements for Electrical Engineers*, Cambridge University Press, Cambridge, 1990.

[88] R. Verfürth, *A posteriori error estimators for the Stokes equations*, Numer. Math., 55 (1989), pp. 309–325.

[89] ——, *A posteriori error estimation and adaptive mesh-refinement techniques*, J. Comp. Appl. Math., 50 (1994), pp. 67–83.

[90] ——, *A Review of A Posteriori Error Estimation and Adaptive Mesh–Refinement Techniques*, Wiley–Teubner, Chichester, 1996.

[91] T. Weiland, *Die Diskretisierung der Maxwell–Gleichungen*, Phys. Bl., 42 (1986), pp. 191–201.

[92] ——, *Time domain electromagnetic field computation with finite difference methods*, Int. J. Num. Model., 9, pp. 295-319 (1996).

[93] J. Whealton, G. Chen, R. Randon, and E. McGaffe, *A 3D analysis of Maxwell's equations for cavities of arbitrary shape*, J. Comput. Phys., 75 (1988), pp. 168–189.

[94] H. Whitney, *Geometric Integration Theory*, Princeton Univ. Press, Princeton, 1957.

[95] B. Wohlmuth, *Hierarchical a posteriori error estimators for mortar finite element methods with Lagrange multipliers*, Tech. Rep. 749, Courant Institute, New York University, 1997.

[96] ——, *A residual based error estimator for mortar finite element discretizations*, Tech. Rep. 370, Math. Inst., University of Augsburg, 1997.

[97] J. Xu, *Iterative methods by space decomposition and subspace correction*, SIAM Review, 34 (1992), pp. 581–613.

[98] K. Yee, *Numerical solution of initial boundary value problems involving Maxwell's equations in isotropic media*, IEEE Trans. Antennas and Propagation, 16 (1966), pp. 302–307.

[99] T. Yiailtsis and T. Tsiboukis, *A ystyematic approach to the construction of higher order vector finite elements for three–dimensional electromagnetic field computation*, COMPEL, 14 (1995), pp. 49–53.

[100] H. Yserentant, *Old and new convergence proofs for multigrid methods*, Acta Numerica, (1993), pp. 285–326.

[101] X. Zhang and K. K. Mei, *Time-domain finite difference approach to the calculation of the frequency-dependent characteristics of microstrip discontinuities*, IEEE Trans. Microw. Theory Tech., 36 (1988).

[102] J. Zhu and O. Zienkiewicz, *Adaptive techniques in the finite element method*, Commun. Appl. Numer. Methods, 4 (1988), pp. 197–204.

[103] O. C. Zienkiewicz and R. L. Taylor, *The Finite Element Method. Basic Formulation and Linear Problems*, vol. 1, McGraw-Hill, London, 1989.